

COHERENT FREQUENCY SHIFTER, OPTICAL ISOLATOR, LASERS ON AN INTEGRATED PLATFORM FOR COLD ATOM MICROSYSTEMS

S. J. Ben Yoo

**Department of Electrical and Computer Engineering
University of California
Davis, CA 95616-8671**

11 October 2017

Final Report

APPROVED FOR PUBLIC RELEASE; DISTRIBUTION IS UNLIMITED.



**AIR FORCE RESEARCH LABORATORY
Space Vehicles Directorate
3550 Aberdeen Ave SE
AIR FORCE MATERIEL COMMAND
KIRTLAND AIR FORCE BASE, NM 87117-5776**

DTIC COPY

NOTICE AND SIGNATURE PAGE

Using Government drawings, specifications, or other data included in this document for any purpose other than Government procurement does not in any way obligate the U.S. Government. The fact that the Government formulated or supplied the drawings, specifications, or other data does not license the holder or any other person or corporation; or convey any rights or permission to manufacture, use, or sell any patented invention that may relate to them.

This report is the result of contracted fundamental research which is exempt from public affairs security and policy review in accordance with AFI 61-201, paragraph 2.3.5.1. This report is available to the general public, including foreign nationals. Copies may be obtained from the Defense Technical Information Center (DTIC) (<http://www.dtic.mil>).

AFRL-RV-PS-TR-2017-0179 HAS BEEN REVIEWED AND IS APPROVED FOR PUBLICATION IN ACCORDANCE WITH ASSIGNED DISTRIBUTION STATEMENT.

//SIGNED//

Dr. Brian Kasch
Program Manager, AFRL/RVBYE

//SIGNED//

Dr. Thomas R. Caudill, Acting Chief
AFRL Battlespace Environment Division

This report is published in the interest of scientific and technical information exchange, and its publication does not constitute the Government's approval or disapproval of its ideas or findings.

REPORT DOCUMENTATION PAGE				Form Approved OMB No. 0704-0188	
Public reporting burden for this collection of information is estimated to average 1 hour per response, including the time for reviewing instructions, searching existing data sources, gathering and maintaining the data needed, and completing and reviewing this collection of information. Send comments regarding this burden estimate or any other aspect of this collection of information, including suggestions for reducing this burden to Department of Defense, Washington Headquarters Services, Directorate for Information Operations and Reports (0704-0188), 1215 Jefferson Davis Highway, Suite 1204, Arlington, VA 22202-4302. Respondents should be aware that notwithstanding any other provision of law, no person shall be subject to any penalty for failing to comply with a collection of information if it does not display a currently valid OMB control number. PLEASE DO NOT RETURN YOUR FORM TO THE ABOVE ADDRESS.					
1. REPORT DATE (DD-MM-YYYY) 11-10-2017		2. REPORT TYPE Final Report		3. DATES COVERED (From - To) 07 Jan 2015 – 22 Jul 2016	
4. TITLE AND SUBTITLE Coherent Frequency Shifter, Optical Isolator, Lasers on an Integrated Platform for Cold Atom Microsystems				5a. CONTRACT NUMBER FA9453-15-1-0006	
				5b. GRANT NUMBER	
				5c. PROGRAM ELEMENT NUMBER 62601F	
6. AUTHOR(S) S. J. Ben Yoo				5d. PROJECT NUMBER 1010	
				5e. TASK NUMBER PPM00035412	
				5f. WORK UNIT NUMBER EF129329	
7. PERFORMING ORGANIZATION NAME(S) AND ADDRESS(ES) Department of Electrical and Computer Engineering University of California Davis, CA 95616-8671				8. PERFORMING ORGANIZATION REPORT NUMBER	
9. SPONSORING / MONITORING AGENCY NAME(S) AND ADDRESS(ES) Air Force Research Laboratory Space Vehicles Directorate 3550 Aberdeen Avenue SE Kirtland AFB, NM 87117-5776				10. SPONSOR/MONITOR'S ACRONYM(S) AFRL/RVBYE	
				11. SPONSOR/MONITOR'S REPORT NUMBER(S) AFRL-RV-PS-TR-2017-0179	
12. DISTRIBUTION / AVAILABILITY STATEMENT Approved for public release; distribution is unlimited.					
13. SUPPLEMENTARY NOTES					
14. ABSTRACT This project report summarizes the UC Davis-led Cold Atom Microsystems (CAMS) project that covers progress on coherent frequency shifter, optical isolator, and lasers at 780 nm wavelength. The LiNbO ₃ based coherent optical frequency shifter worked as a single tone high extinction frequency up shifter/down shifter while it also achieved high extinction optical isolators. The ring laser achieved room temperature cw operations at 780 nm. The summary of the key achievements are as follows: (1) successful experimental demonstration of single tone frequency shifting with extinction 20 dB; (2) experimental demonstration of frequency shifting with continuous sweeping from +/- 2.5 GHz frequency shifts with potential capability to achieve beyond +/- 10 GHz; (3) experimental demonstration achieving frequency shifting with 20 dB optical isolation; (4) experimental demonstration achieving frequency shifting with < 10 % leakage; (5) experimental demonstration achieving frequency shifting with < 3 dB forward optical loss; (6) 29.3 dBm RF power operation of optical frequency shifter; (7) a new design and theoretical analysis of frequency shifter with larger electro-optical coefficients demonstrating 2.85× reduction of required voltage (7.2× power reduction); (8) room temperature cw operation of broad area 780 nm laser fabricated using AlGaAs MQWs bonding wafer stack with InGaP etch stop layer calibrating lasing wavelength and LI-curves; (9) development of AlGaAs active-passive laser fabrication processes including optimized wafer bonding and AlGaAs dry etching recipe; and (10) fabrication of the new 780 nm AlGaAs active-passive integrated laser.					
15. SUBJECT TERMS coherent frequency shifter, optical isolation, integrated photonics, 780nm laser design and fabrication					
16. SECURITY CLASSIFICATION OF:			17. LIMITATION OF ABSTRACT Unlimited	18. NUMBER OF PAGES 68	19a. NAME OF RESPONSIBLE PERSON Dr. Brian Kasch
a. REPORT Unclassified	b. ABSTRACT Unclassified	c. THIS PAGE Unclassified			19b. TELEPHONE NUMBER (include area code)

This page is intentionally left blank.

Table of Contents

I.	EXECUTIVE SUMMARY	1
II.	TECHNICAL APPROACH AND RESULTS	1
II.1.	Frequency shift on LiNbO ₃ and InP	1
II.1.a.	Principle of Operation.....	1
II.1.b.	Electro-optical Rotating Half-Wave Plate in LiNbO ₃	2
II.1.c.	Electro-optical Wave Plates in LiNbO ₃	4
II.1.d.	Electro-optical Wave Plates in Semiconductors with $43m\bar{C}$ Crystal Symmetry.....	6
II.1.e.	Simulation Results and Discussion.....	9
II.2.	Frequency shift, polarization conversion and optical isolation experiment	16
II.2.a.	Polarization Conversion Experiment	16
II.2.b.	Frequency Shifting Experiments	17
II.2.c.	Optical isolation experiment	19
II.2.d.	Theory and experiment on using larger electro-optical coefficient (r_{33} and r_{42})	20
II.3.	780 nm Laser design, fabrication, and testing based on AlGaAs/GaAs Multiple Quantum Wells (MQWs) wafer stack.....	23
II.3.a.	Design and Simulation of MMI coupler based on MQWs wafer stack (all- active).....	24
II.3.b.	Fabrication of Ring cavity laser with MMI couplers.....	27
II.3.c.	Testing results of ring cavity laser	28
II.4.	Design and simulation of active-passive integrated ring cavity laser	31
II.4.a.	AlGaAs MQWs design and simulation	32
II.4.b.	AlGaAs platform ring cavity laser active-passive integration.....	33
III.1.	Publications	52
III.2.	Inventions and Patents	52
III.3.	Students and Postdocs Supported	53
III.4.	Summary.....	53
III.5.	Financial Report	54
	References	55

List of Figures

Figure 1 Frequency shifting of a LHCP light incident on a rotating half-wave plate (RHWP).	2
Figure 2 Simulation result of the spectrum of input and output light after the LiNbO ₃ device showing an increase in carrier frequency after the rotating wave plate.....	6
Figure 3 Device cross section view. (a) Segment 1 with a vertical p-i-n junction to form a wave plate with a 0° angle to the x' axis. (b) Segment 2 with a lateral p-n junction to form a wave plate with 45° angle to the x' axis. (c) Top view of the segments when they are stacked in an alternating order to give a total phase shift equivalent to a half-wave plate.....	8
Figure 4 Input and output polarizations on the Poincare sphere after (a) N=1 segment pairs (b) N=3 segment pairs (c) N=5 segment pairs (d) N=10 segment pairs.....	11
Figure 5 Power loss due to polarization mismatch as a function of the number of segment pairs in the device.	11
Figure 6 The 3D schematic of the frequency shifter device.	12
Figure 7 The top view schematic of the device showing all the segments and the compensation stages. After the 7 segment pairs, there are two compensation stages. Stage 1 is a static quarter wave plate (QWP) with an angle of 45° to the x' axis. Stage 2 is a wave plate with an angle 0° to the x' axis which is modulated out of phase with respect to segment 1.....	12
Figure 8(a) Phase shift of the device after N pairs of segments and without additional stages (b) Phase shift of the device after N pairs of segments and with the additional stages.....	13
Figure 9 Spectrum of the input and output light after 7 segment pairs and additional stages.	13
Figure 10 Side band suppression as a function of the number of segment pairs in the device.....	14
Figure 11(a) Static electric field profile of segment 1 with applied voltage of 3 V. (b) Optical mode profile of segment 1 at $\lambda = 1.55 \mu\text{m}$ wavelength (c) Static electric field profile of segment 2 with applied voltage of 2 V. (d) Optical mode profile of segment 2 at $\lambda = 1.55 \mu\text{m}$ wavelength.	14
Figure 12 LiNbO ₃ based frequency shifter device. The three electrical traces run on top (trace B) and to the left and right of the LiNbO ₃ waveguide (trace C and A). The vertical and horizontal electrical fields can be provided using the three electrical traces.	16
Figure 13 Polarization conversion by applying DC voltage.	17
Figure 14 RF measurement. (a) Experiment diagram. AOM: acoustic optical modulator. (b) Integrated chip with PCB driving circuit. (c-d) Frequency down/up conversion at 100 MHz. (e-f) Frequency down/up conversion at 2 GHz.....	18

Figure 15 Optical isolation experimental diagram.....	19
Figure 16 Single frequency tone conversion, forward transmission.....	19
Figure 17 Optical isolation, backward transmission.....	19
Figure 18 Backward transmission results.	20
Figure 19 (a) Device schematic. (b) Device cross-section and rotation of index ellipsoid for the X-cut, Y-propagating LiTaO ₃ device with applied common and differential voltages to the electrodes.	20
Figure 20(a) TE - TM conversion by applying DC voltage. (b) Spectrum for phase modulation from a sinusoidal driving signal at 20dBm. (c) Measured and theory relative sideband power vs. phase modulation power.	21
Figure 21(a) Experimental diagram using heterodyne detection. (b) 100 MHz up-conversion, 20 dB side lobe suppression. (c) 100 MHz down-conversion, 14 dB side lobe suppression.	22
Figure 22 Band diagrams of GaAs/AlGaAs MQWs laser stack (all-active) with Bias voltage of 0 V, 1.7 V, and 1.75V.	24
Figure 23 Simulated 1x2 MMI coupler based on MQWs wafer stack (all-active) at 780 nm wavelength. The designed MMI width is 10 μm ; length is 225 μm ; two output arms are off-set from center by 2.35 μm	25
Figure 24 Simulated 2x2 MMI coupler based on MQWs wafer stack (all-active) at 780 nm wavelength. The designed MMI width is 15 μm ; length is 650 μm ; two output arms are off-set from center by 2.5 μm ; designed splitting ratio is 50:50.	25
Figure 25 Simulated 2x2 MMI coupler based on MQWs wafer stack (all-active) at 780 nm wavelength. The designed MMI width is 10 μm ; length is 425 μm ; two output arms are off-set from center by 2.5 μm ; designed splitting ratio is 80:15.	26
Figure 26 Design of ring cavity laser with 1x2 MMI coupler.	26
Figure 27 Design of ring cavity laser with 2x2 MMI coupler.	26
Figure 28 Design of double-ring cavity laser with 2x2 MMI couplers.	27
Figure 29 Design of double-ring cavity laser with 2x2 MMI couplers.	27
Figure 30 Layout of designed ring cavity laser with MMI couplers.....	27

Figure 31 Fabrication flow chart (a) initial MQWs wafer and cleaning; (b) Photo lithography; (c) Cl ₂ /BCl ₃ ICP dry etching; (d) PECVD SiO ₂ deposition; (e) BCB spinning; (f) CF ₄ /O ₂ RIE dry etching; (g) BOE release SiO ₂ ; (h) P-contact and N-contact metal lift-off.....	28
Figure 32 Device photos of double-ring cavity laser with MMI couplers.....	28
Figure 33 I-V curve of ring cavity laser.....	29
Figure 34 IdV/dI-I curve of ring cavity laser.....	29
Figure 35 spectrum of ring cavity laser with driving current in CW mode.....	30
Figure 36 L-I curve of ring cavity laser.	30
Figure 37 Spectrum of ring cavity laser with pulsed driving current.	31
Figure 38 Spectrum of straight cavity FP laser with pulsed driving current.	31
Figure 39 Band diagrams of AlGaAs MQWs laser stack for active-passive integration.	32
Figure 40 PL wavelength simulation of the proposed MQWs at 300 K (blue), 400 K (green), 500 K (red).....	32
Figure 41 Simulated material gain of the proposed MQWs at 300 K (blue), 400 K (green), 500 K (red).....	33
Figure 42 Simulated I-V and L-I curve based on a straight cavity FP laser.....	33
Figure 43 (a) device photo of cleaved broad area laser; (b) measurement setup consists of direct probing and cleaved multimode fiber with 50 μ m diameter.....	34
Figure 44 Optical spectrum of broad area laser based by using AlGaAs bonding wafer stack with varying current injection level.	35
Figure 45 (a) output power collected from broad area laser (both facets) with varying driving current and cavity length; (b) output power collected from broad area laser (both facets) with varying driving current density and cavity length.	35
Figure 46 (a-d) output power collected from broad area laser (both facets) with varying driving current and cavity width; (e-h) output power collected from broad area laser (both facets) with varying driving current density and cavity width.	36
Figure 47 AlGaAs MQWs band diagram with Al _{0.05} In _{0.5} Ga _{0.45} P etch stop layer for (a) Ec; (b) Ev.	37
Figure 48 Simulated Ec with Al _{0.05} In _{0.5} Ga _{0.45} P etch stop layer and varying bias voltage	38

Figure 49 SimulatedEv with Al _{0.05} In _{0.5} Ga _{0.45} P etch stop layer and varying bias voltage.	38
Figure 50 Fabrication flow charts of AlGaAs ring cavity laser active-passive integration.....	40
Figure 51 Multiple-stage inverse tapers design top view (top) and cross section (bottom).....	40
Figure 52 Single mode condition of Al _{0.5} Ga _{0.5} As waveguide with SiO ₂ /Al _{0.8} Ga _{0.2} As cladding.	41
Figure 53 TE mode converting of the first inverse taper.	41
Figure 54 TE mode converting of the second inverse taper.	41
Figure 55 Single mode profile and condition of AlGaAs active layers with InGaP undercut current window.	42
Figure 56 3D FDTD simulation of AlGaAs active-passive transmission.....	42
Figure 57 MQWs/core/N-clad to core/N-clad inverse taper transmission with varying inverse taper tip width.	42
Figure 58 Confinement factor and Bending loss simulation of active waveguides for TE ₁ (blue) and TE ₂ (green).	43
Figure 59 Simulation of passive directional coupler and ring coupler with 0.8 μm width.....	43
Figure 60 Active-passive Laser layout overview.....	46
Figure 61 Mask layout of active ring, double ring, unidirectional laser, and active-passive ring.	46
Figure 62 IR image and photo of AlGaAs epi wafer bonded onto 6'' Silicon.	47
Figure 63 BCB bonding system and bonded sample.	47
Figure 64 Direct bonded sample GaAs substrate removal by using wet etching.	47
Figure 65 (a) direct bonded epi-sample after substrate removal; (b)) direct bonded epi-sample after InGaP etch stop layer removal.....	48
Figure 66 SEM photo of ICP dry etched GaAs waveguide with optimized Cl ₂ /BCl ₂ recipe.....	48
Figure 67 Fabricated AlGaAs laser device photos.	49
Figure 68 Device photo of fabricated AlGaAs active-passive transmission section.	49

Figure 69 Fabricated AlGaAs laser bonded on silicon with BCB interface.	49
Figure 70 IV curve a) before; b) after RTP process at 250 °C for 30 seconds.	50
Figure 71 a) The bonded laser device photo with current injection; b) measured L-I curve of the straight cavity AlGaAs bonding laser with BCB interface.	50
Figure 72 Device photos of AlGaAs bonding laser with BCB interface and a) SiO ₂ cladding; b) TiO ₂ cladding.	51
Figure 73 The device photos of ring cavity AlGaAs bonding laser with BCB interface and spectrum collected by vertically mounted multimode cleaved fiber.	51

List of Tables

Table 1 wafer stack description used in this study	8
Table 2 5-QW wafer stack with PL wavelength at 780 nm.	23
Table 3 AlGaAs MQWs wafer stack for active-passive integration.	34
Table 4 Simulated coupling ratio of ring coupler.	43
Table 5 Simulated coupling ratio of directional coupler	45
Table 6 Optimized ICP dry etching of GaAs with Cl ₂ /BCl ₃	48

This page is intentionally left blank.

I. EXECUTIVE SUMMARY

This project report summarizes the UC Davis-led Cold Atom Microsystems (CAMS) project that covers progress on coherent frequency shifter, optical isolator, and lasers at 780 nm wavelength. The LiNbO₃ based coherent optical frequency shifter worked as a single tone high extinction frequency up shifter/down shifter while it also achieved high extinction optical isolators. The ring laser achieved room temperature cw operations at 780 nm. The summary of the key achievements are as follows:

(1) Successful experimental demonstration of single tone frequency shifting with extinction 20 dB, (2) experimental demonstration of frequency shifting with continuous sweeping from +/- 2.5 GHz frequency shifts with potential capability to achieve beyond +/- 10 GHz; (3) experimental demonstration achieving frequency shifting with 20 dB optical isolation; (4) experimental demonstration achieving frequency shifting with < 10 % leakage; (5) experimental demonstration achieving frequency shifting with < 3 dB forward optical loss; (6) 29.3 dBm RF power operation of optical frequency shifter; (7) a new design and theoretical analysis of frequency shifter with larger electro-optical coefficients demonstrating 2.85× reduction of required voltage (7.2× power reduction); (8) Room temperature cw operation of broad area 780 nm laser fabricated using AlGaAs MQWs bonding wafer stack with InGaP etch stop layer calibrating lasing wavelength and LI-curves; (9) Development of AlGaAs active-passive laser fabrication processes including optimized wafer bonding and AlGaAs dry etching recipe; (10) Fabrication of the new 780 nm AlGaAs active-passive integrated laser.

II. TECHNICAL APPROACH AND RESULTS

II.1. Frequency shift on LiNbO₃ and InP

II.1.a. Principle of Operation

Figure 1 illustrates a circularly polarized light wave incident on a rotating half-wave plate. We use a Jones matrix method to show the optical frequency shifting of the incident circularly polarized light. A wave plate is represented by a 2×2 Jones matrix in (1).

$$WP(\psi) = \begin{bmatrix} e^{-i\Gamma/2} \cos^2 \psi + e^{i\Gamma/2} \sin^2 \psi & -i \sin(\Gamma/2) \sin(2\psi) \\ -i \sin(\Gamma/2) \sin(2\psi) & e^{i\Gamma/2} \cos^2 \psi + e^{-i\Gamma/2} \sin^2 \psi \end{bmatrix} \quad (1)$$

where ψ , is the angle between the slow axis of the wave plate and the x -axis (horizontal axis) of the polarization plane of the light which is orthogonal to the propagation direction and Γ is the phase retardation of the wave plate.

$$\Gamma = \frac{2\pi}{\lambda} (n_s - n_f) L \quad (2)$$

where L is the thickness of the wave plate, λ is the wavelength, and n_s and n_f are the refractive indices of slow and fast axes respectively.

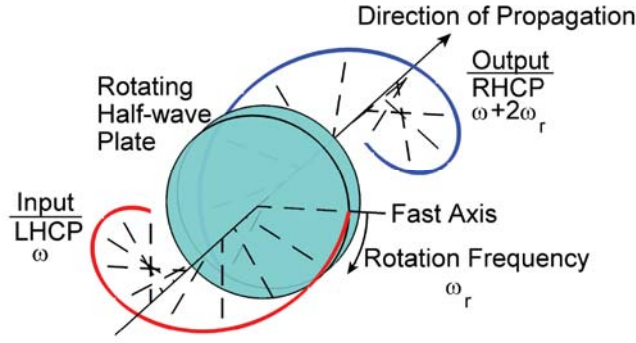


Figure 1 Frequency shifting of a LHCP light incident on a rotating half-wave plate (RHWP).

The phase retardation, Γ , is equal to π for a half-wave plate. The angle ψ is equal to $\omega_r t$ for a wave plate rotating counter clockwise with a frequency of ω_r viewing from the light source and t is the time. Then, we can express the Jones matrix for a rotating half-wave plate (RHWP) as in (3).

$$RHWP(\omega_r) = e^{-i\pi/2} \begin{bmatrix} \cos(2\omega_r t) & \sin(2\omega_r t) \\ \sin(2\omega_r t) & -\cos(2\omega_r t) \end{bmatrix} \quad (3)$$

Left hand circularly polarized waves (LHCP) and the right hand circularly polarized waves (RHCP) with an optical frequency of ω by 1×2 Jones as given in (4) and (5).

$$LHCP(\omega) = \frac{1}{\sqrt{2}} \begin{bmatrix} 1 \\ i \end{bmatrix} e^{i\omega t} \quad (4)$$

$$RHCP(\omega) = \frac{1}{\sqrt{2}} \begin{bmatrix} 1 \\ -i \end{bmatrix} e^{i\omega t} \quad (5)$$

If we assume that a LHCP wave is incident on a RHWP rotating in the clockwise direction and calculate the output as shown in- (6).

$$\begin{aligned} \text{Output} &= RHWP(\omega_r) LHCP(\omega) \\ &= e^{-i\pi/2} \begin{bmatrix} \cos(2\omega_r t) & \sin(2\omega_r t) \\ \sin(2\omega_r t) & -\cos(2\omega_r t) \end{bmatrix} \frac{1}{\sqrt{2}} \begin{bmatrix} 1 \\ i \end{bmatrix} e^{i\omega t} = e^{-i\pi/2} \frac{1}{\sqrt{2}} \begin{bmatrix} 1 \\ -i \end{bmatrix} e^{i(\omega+2\omega_r)t} \\ &= e^{-i\pi/2} RHCP(\omega + 2\omega_r) \end{aligned} \quad (6)$$

In this case, the direction of the rotation of the RHWP is in the opposite sense with respect to the polarization of incident circularly polarized wave, so the frequency of the output wave is increased by twice the rotation frequency of the half-wave plate and the output polarization becomes RHCP.

When the direction of the rotation of the half-wave plate is in the same sense with the polarization of the incident circularly polarized wave, the frequency of the output wave is decreased by twice the rotation frequency of the half-wave plate.

II.1.b. *Electro-optical Rotating Half-Wave Plate in LiNbO₃*

It is possible to emulate a rotating half-wave plate by optical index modulation using Pockels effect in some electro-optical materials. In [1], a Ti-diffused waveguide in an x -cut z -propagating

LiNbO₃ device was used to realize an electro-optical rotating half-wave plate. In quadrature electric fields in x and y directions were applied to the waveguide using three electrodes. In this section, we investigate the index changes for the device in [1] under in quadrature electric fields.

The electro-optic tensor of LiNbO₃ is represented by the 6×3 matrix in (7).

$$\Delta\left(\frac{1}{n^2}\right) = \begin{bmatrix} 0 & -r_{22} & r_{13} \\ 0 & r_{22} & r_{13} \\ 0 & 0 & r_{33} \\ 0 & r_{42} & 0 \\ r_{42} & 0 & 0 \\ -r_{22} & 0 & 0 \end{bmatrix} \begin{bmatrix} E_x \\ E_y \\ E_z \end{bmatrix} \quad (7)$$

where the coefficient r is called Pockels coefficient. The refractive index is modified linearly with the applied electric field in x , y , and z -directions represented by the subscripts 1, 2, and 3 due to Pockels effect according to (8). The subscripts 4, 5 and 6 represent off diagonal elements in yz , zx and xy -directions.

$$\Delta\left(\frac{1}{n^2}\right)_i = \sum_{j=1}^3 r_{ij} E_j \quad (8)$$

Then using (7) and (8), we write the index ellipsoid equation or the indicatrix for LiNbO₃ as shown in (9), when there are electric fields applied in x , y , and z -directions.

$$\begin{aligned} & x^2 \left(\frac{1}{n_o^2} - r_{22} E_y + r_{13} E_z \right) + y^2 \left(\frac{1}{n_o^2} + r_{22} E_y + r_{13} E_z \right) + z^2 \left(\frac{1}{n_e^2} + r_{33} E_z \right) \\ & + 2r_{42} E_y yz + 2r_{42} E_x xz - 2r_{22} E_x xy = 1 \end{aligned} \quad (9)$$

If the electric fields in [1] are applied in only the x and y -directions, we can further reduce the index ellipsoid equation by assigning the electric field in the z -direction to 0, propagation in the z -direction, and considering the equation only in the xy -plane.

$$x^2 \left(\frac{1}{n_o^2} - r_{22} E_y \right) + y^2 \left(\frac{1}{n_o^2} + r_{22} E_y \right) - 2r_{22} E_x xy = 1 \quad (10)$$

The cross term in (10) indicates there is a rotation of principle axes of the system around the z -axis. As a coordinate transformation, we can assume that the axes are rotated clockwise by an angle θ around the z -axis and define new principle axes, x' , y' , and z' as given in (11) and (12).

$$x = x' \cos(\theta) - y' \sin(\theta) \quad (11)$$

$$y = x' \sin(\theta) + y' \cos(\theta) \quad (12)$$

Using (10), (11) and (12), we can write the index ellipsoid in the x' , y' , and z' coordinates as given in (13).

$$\begin{aligned}
& x'^2 \left[\cos^2 \theta \left(\frac{1}{n_o^2} - r_{22} E_y \right) + \sin^2 \theta \left(\frac{1}{n_o^2} + r_{22} E_y \right) - r_{22} E_x \sin(2\theta) \right] \\
& + y'^2 \left[\sin^2 \theta \left(\frac{1}{n_o^2} - r_{22} E_y \right) + \cos^2 \theta \left(\frac{1}{n_o^2} + r_{22} E_y \right) + r_{22} E_x \sin(2\theta) \right] \\
& + x' y' \left[-2r_{22} E_x \cos(2\theta) + 2r_{22} E_y \sin(2\theta) \right] = 1
\end{aligned} \tag{13}$$

We can make the coefficient of the cross term in (13) equal to 0 when θ value satisfies eqn. (14). Then we can form the relation given in (14) between the rotation of the principle axes and the applied electric fields.

$$\frac{\cos(2\theta)}{\sin(2\theta)} = \frac{E_y}{E_x} \tag{14}$$

Since the electric fields are applied in quadrature, we can express the electric fields in x and y directions as in (15) and (16).

$$E_x = E_0 \sin(\omega_d t) \tag{15}$$

$$E_y = E_0 \cos(\omega_d t) \tag{16}$$

where ω_d is the frequency of the applied sine wave. Using (14), (15) and (16), we find that the rotation angle of the slow and fast axes of the wave plate can be expressed as a function of time as shown in (17).

$$\theta = \frac{\omega_d t}{2} \tag{17}$$

We can also find the refractive index changes in slow and fast axes of the wave plate using (13).

$$n_{x'} \approx n_0 + \frac{n_0^3 r_{22} (E_x \sin(2\theta) + E_y \cos(2\theta))}{2} \tag{18}$$

$$n_{y'} \approx n_0 - \frac{n_0^3 r_{22} (E_x \sin(2\theta) + E_y \cos(2\theta))}{2} \tag{19}$$

We find that the index difference, Δn , between the slow and fast axes of the wave plate is independent of time as given in (20).

$$\Delta n = n_{x'} - n_{y'} = \frac{n_0^3}{2} r_{22} (2E_0 \cos(2\theta - \omega_d t)) = n_0^3 r_{22} E_0 \tag{20}$$

The fast and slow axes of the wave plate are rotating with a frequency of $\omega_d/2$ and by choosing the length of the device as $\lambda/(2n_0^3 r_{22} E_0)$, a rotating half-wave plate was formed in LiNbO₃ electro-optically. Since the rotation frequency of the wave plate is half of the frequency of the driving electric fields, the magnitude of frequency shift is expected to be ω_d .

II.1.c. *Electro-optical Wave Plates in LiNbO₃*

It is useful to analyze the individual effects of electric fields applied from x and y-directions in LiNbO₃. We can write the index ellipsoid of an x-cut z-propagating LiNbO₃ device as in (21) when the electric field is applied in the y-direction.

$$x^2 \left(\frac{1}{n_o^2} - r_{22} E_y \right) + y^2 \left(\frac{1}{n_o^2} + r_{22} E_y \right) = 1 \quad (21)$$

From (22) and (23), we find the refractive indices of the slow and fast axes of the wave plate as in (23).

$$n_x \approx n_o + \frac{n_o^3}{2} r_{22} E_y \quad (22)$$

$$n_y \approx n_o - \frac{n_o^3}{2} r_{22} E_y \quad (23)$$

The slow and fast axes are on x and y -axes of the system, thus, it suggests that applying an electric field in the y -direction forms a wave plate with slow axis at an angle of 0° to the x -axis. Using (22) and (23), we find the index difference between fast and slow axes as in (24).

$$\Delta n = n_x - n_y = n_o^3 r_{22} E_y \quad (24)$$

When the electric field is applied in the x -direction, we can write the index ellipsoid as in (25).

$$x^2 \left(\frac{1}{n_o^2} \right) + y^2 \left(\frac{1}{n_o^2} \right) - 2r_{22} E_x xy = 1 \quad (25)$$

The cross term, xy , in (25) suggests that we can rotate the principal axes counter-clockwise by 45° with the coordinate transformation given in (26) and (27).

$$x = \frac{x' - y'}{\sqrt{2}} \quad (26)$$

$$y = \frac{x' + y'}{\sqrt{2}} \quad (27)$$

Then, we rewrite the index ellipsoid equation in the new coordinates as in (28).

$$x'^2 \left(\frac{1}{n_o^2} - r_{22} E_x \right) + y'^2 \left(\frac{1}{n_o^2} + r_{22} E_x \right) = 1 \quad (28)$$

From (28), we find the refractive indices of slow and fast axes of the wave plate as in (29) and (30).

$$n_{x'} \approx n_o + \frac{n_o^3}{2} r_{22} E_x \quad (29)$$

$$n_{y'} \approx n_o - \frac{n_o^3}{2} r_{22} E_x \quad (30)$$

The slow and fast axes are on x' and y' -axes of the system, which have a 45° angle with respect to the xy -plane of the system. Thus applying an electric field in the x -direction forms a wave plate with slow axis at a 45° angle to the x -axis. Using (29) and (30), we find the index difference between the slow and fast axes as in (31).

$$\Delta n = n_{x'} - n_{y'} = n_0^3 r_{22} E_x \quad (31)$$

Thus, forming wave plates with 45° and 0° angle to the x -axis and modulating refractive indices of the slow and fast axes of those wave plates by in quadrature electric fields forms a rotating half-wave plate in LiNbO₃. The same principle can also be applied to a semiconductor material platform with $\bar{4}3m$ crystal symmetry if wave plates with 45° and 0° angle can be formed using Pockels effect and modulated in the same way as in the LiNbO₃ case.

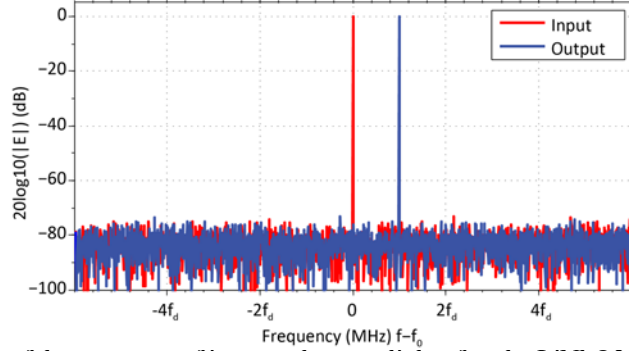


Figure 2 Simulation result of the spectrum of input and output light after the LiNbO₃ device showing an increase in carrier frequency after the rotating wave plate.

Figure 8 shows the result of the simulation of the spectrum of the input and output light wave for the LiNbO₃ rotating half-wave plate frequency shifter device. The single tone input light propagates through the rotating half waveplate mentioned in II.1.a. and II.1.b and the output light frequency is shifted by the modulation frequency f_d of the applied electric fields, which is 200 MHz in the simulation. The result shows that the frequency of the output wave is 200 MHz upshifted compared to the input wave and there are no side-bands. White Gaussian noise at the noise level of -80 dBm is added onto the signal.

II.1.d. *Electro-optical Wave Plates in Semiconductors with $\bar{4}3m$ Crystal Symmetry*

This section presents a theoretical analysis of frequency shifter using semiconductors with $\bar{4}3m$ crystal symmetry. The electro-optic tensor for materials with $\bar{4}3m$ crystal symmetry is represented by the 6×3 matrix given in (32).

$$\Delta \left(\frac{1}{n^2} \right) = \begin{bmatrix} 0 & 0 & 0 \\ 0 & 0 & 0 \\ 0 & 0 & 0 \\ r_{41} & 0 & 0 \\ 0 & r_{41} & 0 \\ 0 & 0 & r_{41} \end{bmatrix} \begin{bmatrix} E_x \\ E_y \\ E_z \end{bmatrix} \quad (32)$$

The crystal directions $[100]$, $[010]$ and $[001]$ are represented as x , y , and z coordinates respectively. To form wave plates with 0° and 45° angle, we suggest cleaving the waveguide facet with a 45° angle on a wafer with a surface normal direction of $[001]$ and the waveguide direction is chose as the $[\bar{1}10]$ direction. The $[110]$, $[\bar{1}10]$, and $[001]$ directions are represented as x' , y' and z' directions. The waveguide facet lies in $x'z'$ -plane and the waveguide propagation direction is y' . In the new crystal orientation, we can write the electro-optic tensor in an updated coordinate system as in (33).

$$\Delta\left(\frac{1}{n^2}\right) = \begin{bmatrix} 0 & 0 & r_{41} \\ 0 & 0 & -r_{41} \\ 0 & 0 & 0 \\ 0 & -r_{41} & 0 \\ r_{41} & 0 & 0 \\ 0 & 0 & 0 \end{bmatrix} \begin{bmatrix} E_{x'} \\ E_{y'} \\ E_{z'} \end{bmatrix} \quad (33)$$

Then, we write the index ellipsoid equation as in (34).

$$\begin{aligned} x'^2 \left(\frac{1}{n_0^2} + r_{41} E_{z'} \right) + y'^2 \left(\frac{1}{n_0^2} - r_{41} E_{z'} \right) + z'^2 \left(\frac{1}{n_0^2} \right) \\ - 2r_{41} E_{y'} y' z' + 2r_{41} E_{x'} x' z' = 1 \end{aligned} \quad (34)$$

We first consider the case where the electric field is applied in the z' direction. Since the waveguide facet is on the $x'z'$ plane, we can reduce the index ellipsoid to (35).

$$x'^2 \left(\frac{1}{n_0^2} + r_{41} E_{z'} \right) + z'^2 \left(\frac{1}{n_0^2} \right) = 1 \quad (35)$$

Using (35), we find the refractive indices of the slow and fast axis of the wave plate formed in the crystal as in (36) and (37).

$$n_{x'} \approx n_0 - \frac{n_0^3}{2} r_{41} E_{z'} \quad (36)$$

$$n_{z'} \approx n_0 \quad (37)$$

Since the slow and fast axes coincide with $x'z'$ plane, we can conclude that applying an electric field in the z' direction creates a wave plate with 0° angle to the system axes. We find the index difference between slow and fast axes as in (38). Note that in contrast with the LiNbO_3 case, this waveplate has half of the index change, and is not a differential modulation in both axes. This will be important as it contributes an additional phase chirp.

$$\Delta n = n_{z'} - n_{x'} = \frac{n_0^3}{2} r_{41} E_{z'} \quad (38)$$

Second, we consider the case where the electric field is applied in the x' direction. Again, the waveguide facet is on the $x'z'$ plane and we can reduce the index ellipsoid to (39).

$$x'^2 \left(\frac{1}{n_0^2} \right) + z'^2 \left(\frac{1}{n_0^2} \right) + 2r_{41} E_{x'} x' z' = 1 \quad (39)$$

We can rotate the principal axes counter-clockwise by 45° around the y' axis and eliminate the cross term in (39) with the coordinate transformation in (40) and (41).

$$x' = \frac{x'' - z''}{\sqrt{2}} \quad (40)$$

$$z' = \frac{x'' + z''}{\sqrt{2}} \quad (41)$$

We rewrite the index ellipsoid in the new coordinates as in (42).

$$x''^2 \left(\frac{1}{n_0^2} + r_{41} E_{x'} \right) + z''^2 \left(\frac{1}{n_0^2} - r_{41} E_{x'} \right) = 1 \quad (42)$$

Then, we find the refractive indices of the slow and fast axis of the wave plate formed in the crystal as in (43) and (44).

$$n_{x''} \approx n_0 - \frac{n_0^3}{2} r_{41} E_{x'} \quad (43)$$

$$n_{z''} \approx n_0 + \frac{n_0^3}{2} r_{41} E_{x'} \quad (44)$$

We can conclude that applying an electric field in the x' forms a wave plate with 45° angle to the $x'z'$ plane. We also find the index difference between fast and slow axis as in (45) using (43).

$$\Delta n = n_{z''} - n_{x''} = n_0^3 r_{41} E_{x'} \quad (45)$$

To apply an electric field in x' and z' directions to a waveguide in a semiconductor material with p - n or p - i - n junctions, we propose two types of segments in the device. Figure 3(a) shows that Segment 1 has a vertical junction to apply an electric field in the z' direction and Figure 3 (b) shows that Segment 2 has a lateral junction to apply an electric field in x' . To fabricate this device from a single type of wafer stack in the form of a vertical p - i - n junction as described in Table 1, selective ion implantation can be used to form the lateral p - n junction segments.

If the segments are stacked in a sufficient number of pairs in an alternating fashion as shown in Figure 3 (c), a good approximation to an endlessly rotating wave plate can be achieved. When the lengths of each segment are adjusted to give a total phase retardation of π , a half-wave plate can be formed.

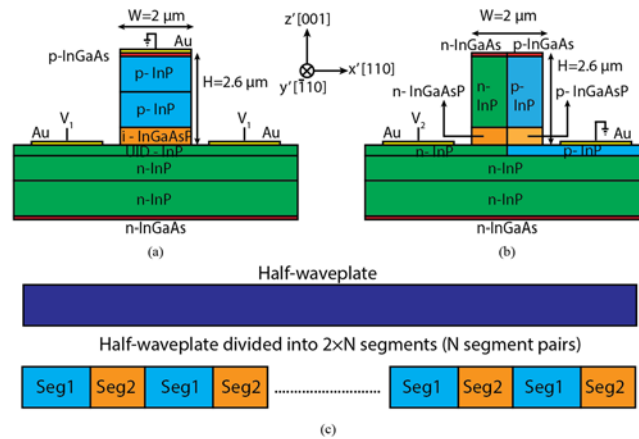


Figure 3 Device cross section view. (a) Segment 1 with a vertical p-i-n junction to form a wave plate with a 0° angle to the x' axis. (b) Segment 2 with a lateral p-n junction to form a wave plate with 45° angle to the x' axis. (c) Top view of the segments when they are stacked in an alternating order to give a total phase shift equivalent to a half-wave plate.

TABLE 1 Wafer Stack Description used in this Study

Layer	Material	In	Ga	As	P	Height (μm)	Doping (/cm ³)
p-	InGaAs	0.53	0.47	1	0	0.1	2E+18

TABLE 1 Wafer Stack Description used in this Study (continued)

contact							
p-clad	InP	1	0	0	1	1	5E+17
p-clad	InP	1	0	0	1	1	1E+17
WG	InGaAsP	0.81	0.19	0.4	0.6	0.5	UID
i-clad	InP	1	0	0	1	0.3	UID
n-clad	InP	1	0	0	1	0.7	1E+17
n-clad	InP	1	0	0	1	1	5E+17
n- contact	InGaAs	0.53	0.47	1	0	0.1	1E+18

II.1.e. *Simulation Results and Discussion*

II.1.e.i. *Analysis of the System using Jones Calculus*

The system with N pairs of wave plates is investigated using Jones matrix calculus to determine the optimum number of segments. The Jones matrices for segment 1 and segment 2 can be found using the general equation for a wave plate with slow axis index of n_s , fast axis index of n_f , with a length of L , and with an angle ψ to the principle axes of the system given in (46).

$$\begin{bmatrix} E_{x'}^{out} \\ E_{z'}^{out} \end{bmatrix} = R(-\psi) \begin{bmatrix} e^{-in_s \frac{2\pi}{\lambda} L} & 0 \\ 0 & e^{-in_f \frac{2\pi}{\lambda} L} \end{bmatrix} R(\psi) \begin{bmatrix} E_{x'}^{in} \\ E_{z'}^{in} \end{bmatrix} \quad (46)$$

The rotation matrix $R(\psi)$ is for rotating the slow and fast axis of the wave plates to the principle axes of the system and it is given by (47).

$$R(\psi) = \begin{bmatrix} \cos(\psi) & \sin(\psi) \\ -\sin(\psi) & \cos(\psi) \end{bmatrix} \quad (47)$$

To have the total phase shift of a half-wave plate after N pairs of segments, each segment is designed to have a phase retardation of π/N . The refractive index change of the slow axis and fast axis of the wave plate formed in segment 1 and segment 2 due to Pockels effect was found in (38) and (45). All segment 1s are driven with the cosine fields, and all segment 2s are drive with the sine fields. If in quadrature electric fields are applied to those segments, the phase retardation of segments is given in (48) and (49).

$$\begin{aligned} \Gamma_1 &= \frac{2\pi}{\lambda} \Delta n_1 L_1 = \frac{2\pi}{\lambda} \frac{n_0^3}{2} r_{41} E_{z'}(t) L_1 = \frac{\pi}{\lambda} n_0^3 r_{41} E_1 \cos(\omega_d t) L_1 \\ &= \frac{\pi}{N} \cos(\omega_d t) \end{aligned} \quad (48)$$

$$\begin{aligned} \Gamma_2 &= \frac{2\pi}{\lambda} \Delta n_2 L_2 = \frac{2\pi}{\lambda} n_0^3 r_{41} E_{x'}(t) L_2 = \frac{2\pi}{\lambda} n_0^3 r_{41} E_2 \sin(\omega_d t) L_2 \\ &= \frac{\pi}{N} \sin(\omega_d t) \end{aligned} \quad (49)$$

The Jones matrices for segment 1 and segment 2 are also given in (50)

$$\begin{aligned}
Seg_1 &= R(0^\circ) \begin{bmatrix} e^{-i\left(n_0 - \frac{n_0^3}{2} r_{41} E_x\right) \frac{2\pi}{\lambda} L_1} & 0 \\ 0 & e^{-in_0 \frac{2\pi}{\lambda} L_1} \end{bmatrix} R(0^\circ) \\
&= e^{-in_0 \frac{2\pi}{\lambda} L_1} \begin{bmatrix} e^{i\frac{\pi}{N} \cos(\omega_d t)} & 0 \\ 0 & 1 \end{bmatrix}
\end{aligned} \tag{50}$$

$$\begin{aligned}
Seg_2 &= R(-45^\circ) \begin{bmatrix} e^{-i\left(n_0 - \frac{n_0^3}{2} r_{41} E_x\right) \frac{2\pi}{\lambda} L_2} & 0 \\ 0 & e^{-i\left(n_0 + \frac{n_0^3}{2} r_{41} E_x\right) \frac{2\pi}{\lambda} L_2} \end{bmatrix} R(45^\circ) \\
&= e^{-in_0 \frac{2\pi}{\lambda} L_2} \begin{bmatrix} \cos\left(\frac{\pi}{2N} \sin(\omega_d t)\right) & i \sin\left(\frac{\pi}{2N} \sin(\omega_d t)\right) \\ i \sin\left(\frac{\pi}{2N} \sin(\omega_d t)\right) & \cos\left(\frac{\pi}{2N} \sin(\omega_d t)\right) \end{bmatrix}
\end{aligned} \tag{51}$$

The output Jones vector of the system can be written by

$$\underline{Output} = \left[\underline{Seg_2 Seg_1} \right]^N \underline{Input} \tag{52}$$

The output polarization vectors were calculated with respect to one modulation period using MATLAB and plots were generated. The polarization of the output over one modulation period is shown on the Poincare sphere for different numbers of segment pairs in Figure 4. Here, the analysis assumes LHCP as the input polarization to the system. In this case, the output polarization for an ideal rotating half-wave plate should be RHCP. Figure 4 shows that the output polarization is varying in one modulation period and the approximation to a half-wave plate gets better with the increasing number of segment pairs. We estimate the power loss due to the polarization mismatch by calculating the polarization loss factor (PLF) which is the dot product of Jones vectors of the target polarization and the time varying output polarization vector as given in (53).

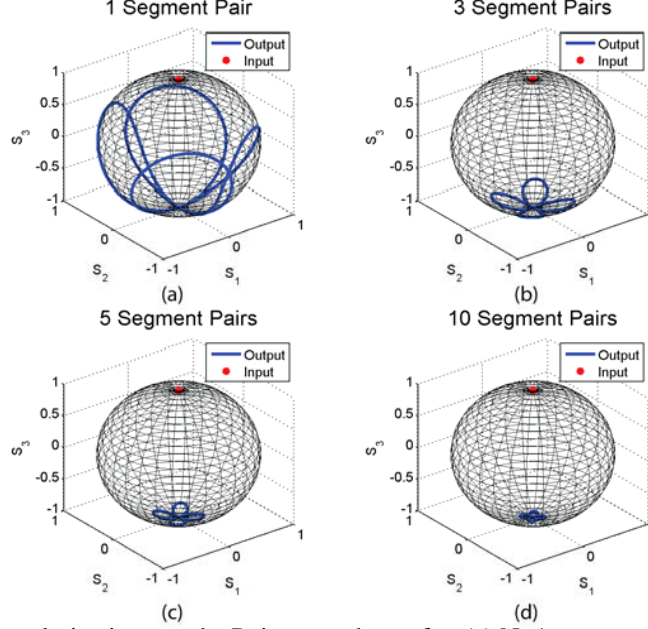


Figure 4 Input and output polarizations on the Poincare sphere after (a) N=1 segment pairs (b) N=3 segment pairs (c) N=5 segment pairs (d) N=10 segment pairs.

$$PLF = \left| \frac{RHCP \cdot Output}{Input} \right|^2 \quad (53)$$

$$P_{Loss} = -10 \log_{10}(PLF)$$

Figure 5 shows the maximum power loss in time as a function of segment pairs.

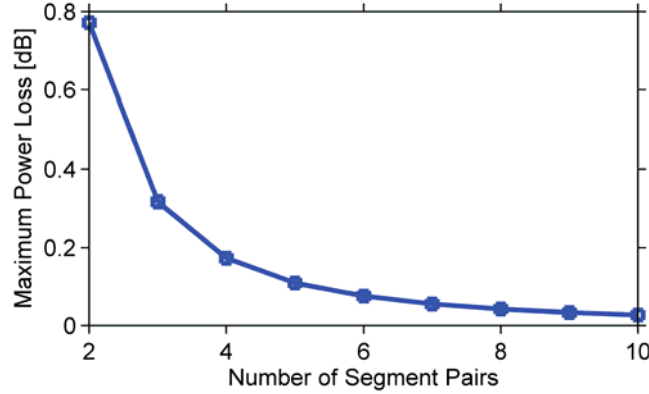


Figure 5 Power loss due to polarization mismatch as a function of the number of segment pairs in the device.

To have the minimum polarization mismatch loss and high side band suppression with the least number of segment pairs, we have 7 segment pairs in the system. The maximum power loss due to polarization mismatch is 0.055 dB for 7 segment pairs.

II.1.e.ii. **Reduction of the Phase Wobble with Compensation Stages**

In (36), we can see that the refractive indices on the principle axes of the wave plate formed in segment 1 can be modulated in only one of the axes. However, in the LiNbO₃ frequency shifter device, the index modulation is present on both of the orthogonal axes as in (22), (23), (29) and (30). Since the waveplate formed in segment 1 is not a differential wave plate, there is a phase wobble in the total phase shift after N pairs of segments. To address the wobbling issue, we design the following structure. Figure 6 and Figure 7 show the 3D view and top view of all the segments in the device design respectively. The first compensation stage is a quarter wave plate (QWP) with

an angle of 45° . This stage can be put into the stack by making a lateral junction device with the same structure as segment 2 and applying a DC voltage. The second additional stage is a variable delay wave plate with an angle of 0° to the x' axes, which the index modulation is out of phase with the index modulation of the segment 1. After N segment pairs, the LHCP light is converted to a RHCP light, since N segment pairs approximate a half-wave plate. The quarter wave plate (QWP) converts the RHCP light into linear polarized (LP) light along x' axis ($LP_{x'}$). After that, the variable delay wave plate cancels out the accumulated effect from all segment 1s.

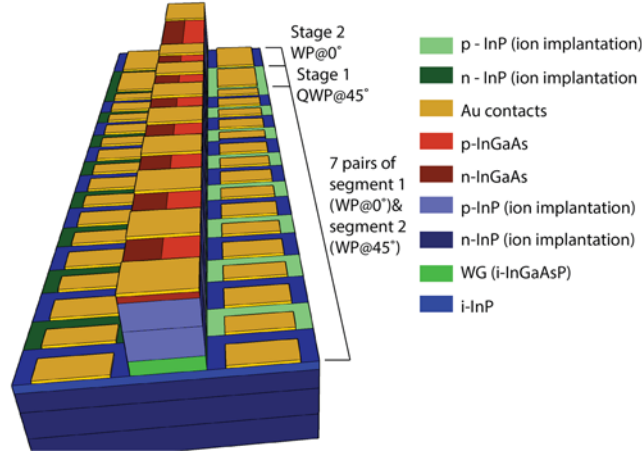


Figure 6 The 3D schematic of the frequency shifter device.

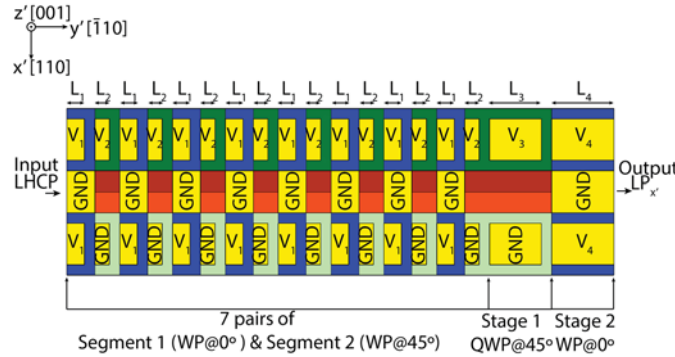


Figure 7 The top view schematic of the device showing all the segments and the compensation stages. After the 7 segment pairs, there are two compensation stages. Stage 1 is a static quarter wave plate (QWP) with an angle of 45° to the x' axis. Stage 2 is a wave plate with an angle 0° to the x' axis which is modulated out of phase with respect to segment 1.

Figure 8 shows the effect of compensation stages on the phase accumulation at the output. As shown in Figure 8 (a), the phase accumulation is not linear in time as it would be expected from a single-side frequency shifting system, but there is an oscillation or phase wobble. To reduce this effect, two compensation stages are inserted after N pairs of segments. Figure 8 (b) shows the phase accumulation at the output with the additional stages of a stationary quarter wave plate and variable delay wave plate added to the system. The phase accumulation is linear in time and there is no phase wobble.

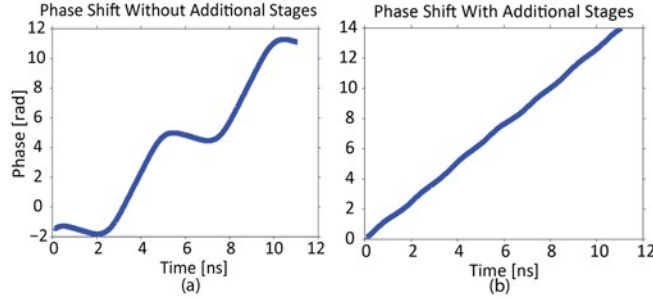


Figure 8(a) Phase shift of the device after N pairs of segments and without additional stages (b) Phase shift of the device after N pairs of segments and with the additional stages.

Figure 9 shows the spectrum analysis of the input and output electric field for 7 segment pairs. The side band suppression is more than 40 dB and the difference between the maximum peaks is only 0.027 dB. The frequency of the driving voltage is chosen as 200 MHz in this case and the frequency is upshifted by the frequency of the driving voltage. There are side bands at $f_0 - 3f_d$ and $f_0 + 5f_d$. The noise level is at -80 dBm.

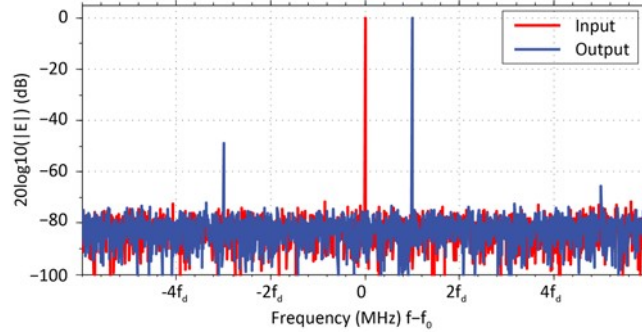


Figure 9 Spectrum of the input and output light after 7 segment pairs and additional stages.

Figure 10 shows the side band suppression as a function of the number of segment pairs.

II.1.e.iii. *Optical Mode Profile and Electric Field Profile*

Figure 11 (a) and (c) show the simulated optical mode profile of the vertical and horizontal p-n junction devices respectively. The waveguides are designed to give mode match between segments and also to minimize the modal birefringence between the TE and TM modes. We calculate that the mode overlap integral between the optical modes of two segments is 0.9945, which results in 0.024 dB insertion loss for the transition between segments. The system has 16 junctions where segment 1 and segment 2 join with one another, which gives a total mode mismatch loss of 0.38 dB. Figure 11 (b) and (d) show the electric field profile of the vertical and horizontal p-n junction devices respectively when they are reverse biased with an applied 3 V and 2 V DC voltage. The electric field profile was simulated by solving the Laplace equation for the device. We calculate the electro-optic overlap factor by calculating the overlap integral given in (54). The electric field profiles in x' and z' directions are denoted by $E_{x'}$ and $E_{z'}$ respectively. The optical field is denoted by E_{opt} .

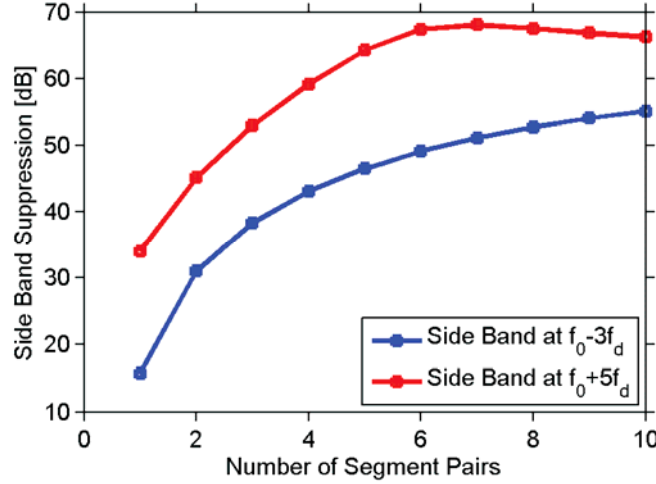


Figure 10 Side band suppression as a function of the number of segment pairs in the device.

$$\Gamma = \frac{\iint_{Area} |E_{opt}(x', z')|^2 E_{x',z'}(x', z') dx' dz'}{\iint_{Area} |E_{opt}(x', z')|^2 dx' dz'} \quad (54)$$

Using the electro-optic overlap factor we calculate the DC $V_\pi \cdot L$ product for each segment using (55).

$$V_\pi \cdot L = \frac{\lambda}{n_o^3 r_{41} \Gamma} \quad (55)$$

We find the DC $V_\pi \cdot L$ product as 1.03 V·cm and 1.42 V·cm for segment 1 and segment 2 respectively. In the LiNbO₃ frequency shifter device demonstrated in [1] the $V_\pi \cdot L$ products were 26 V·cm and 31 V·cm for horizontal and vertical fields respectively. In the AlGaAs/GaAs based frequency shifter demonstrated in [2], the $V_\pi \cdot L$ products were 3.33 V·cm and 4.33 V·cm for horizontal and vertical electric fields respectively

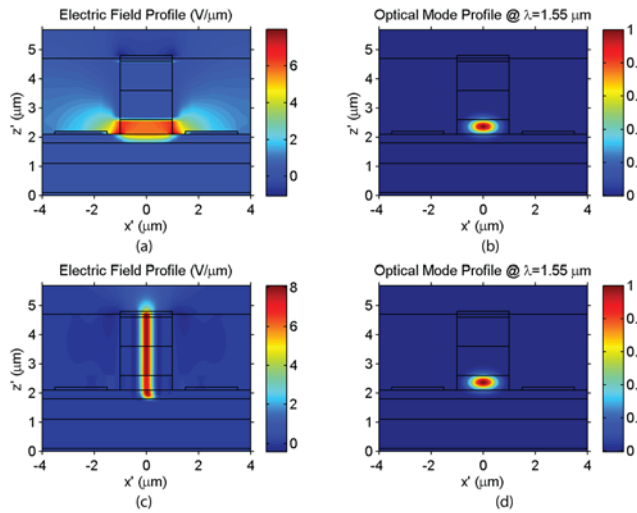


Figure 11(a) Static electric field profile of segment 1 with applied voltage of 3 V. (b) Optical mode profile of segment 1 at $\lambda = 1.55 \mu\text{m}$ wavelength (c) Static electric field profile of segment 2 with applied voltage of 2 V. (d) Optical mode profile of segment 2 at $\lambda = 1.55 \mu\text{m}$ wavelength.

The effective electric fields due to the overlap integral of the electric field profile and optical mode profile for segment 1 and segment 2 are 5.2×10^6 V/m and 3.1×10^6 V/m, respectively. Using this, we find the applied voltages to the device to achieve frequency shifting as shown in (56).

$$\begin{aligned}
V_1(t) &= V_{DC1} + V_{01} \cos(\omega_r t) = V_{DC} + 3 \cos(\omega_r t) \\
V_2(t) &= V_{DC2} + V_{02} \sin(\omega_r t) = V_{DC} + 2 \sin(\omega_r t) \\
V_3(t) &= V_{DC3} = 2 \text{ V} \\
V_4(t) &= V_{DC4} + V_{04} \cos(\omega_r t) = V_{DC} - 3 \cos(\omega_r t)
\end{aligned} \tag{56}$$

The DC voltages represented as V_{DC} ensure that the junctions are in reverse bias at all times. So we assume that they are larger than 6 V. We find that the lengths of the segments as $L_1 = 851$ μm , $L_2 = 716$ μm , $L_3 = 2.51$ mm, $L_4 = 2.98$ mm. The total length of the device is 16.46 mm. One thing we should notice is that the DC voltage will have an additional static waveplate transformation. We would need to introduce intentional modal birefringence in the waveguide design to compensate for the electro-optical birefringence induced by the DC voltages.

II.2. Frequency shift, polarization conversion and optical isolation experiment

II.2.a. Polarization Conversion Experiment

The LiNbO₃ device orientation is X-cut Z-propagation waveguide, where the z-axis is the optical axis and the plane perpendicular to the z-axis is isotropic. The birefringence between vertical and horizontal polarized light can be minimized in this way. The insertion loss of the device is about 4 dB. The facet edge of the device is not perpendicular (8.7°) to the other edges to reduce the reflection.

Figure 12 shows the device structure. The waveguide region are diffused with ZnO (ZnO-LiNbO₃) to change the refractive index and confine the light. There are three electrical traces (A, B and C). The trace B is right on top of the ZnO-LiNbO₃ waveguide and trace C and A are to the left and right of the waveguide respectively. By applying common voltage trace A and C and making B the ground, we will generate a vertical field in the waveguide region; similarly, applying a differential field on A and C will provide a horizontal field. Given that the device is X-cut Z-propagate, the voltage configuration determines what electro-optic coefficients will be used.

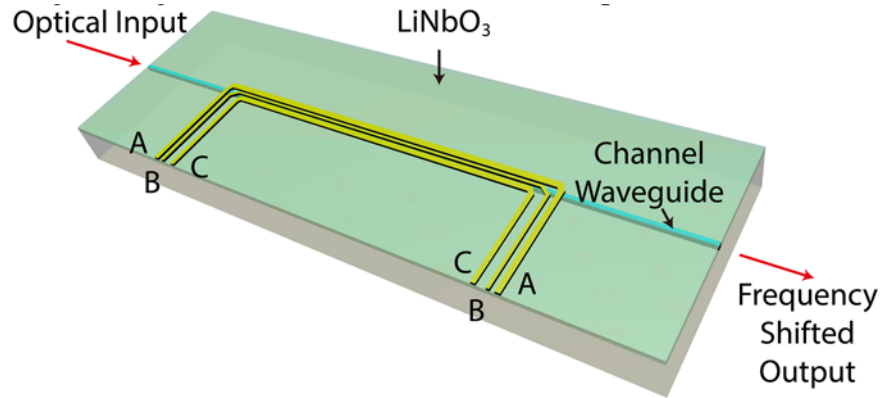


Figure 12 LiNbO₃ based frequency shifter device. The three electrical traces run on top (trace B) and to the left and right of the LiNbO₃ waveguide (trace C and A). The vertical and horizontal electrical fields can be provided using the three electrical traces.

To characterize the electro-optic effect of the device, we conduct the polarization conversion experiment in the first place. Figure 13(a) shows the experiment setup where we send the light from a 780 nm external cavity laser (ECL) to the device and there is a polarization controller (PC) to adjust the input polarization. A polarization beam splitter (PBS) splits the two different polarizations to be detected by two power meters. We first make sure that all the input is TE-polarized. Then we apply the same voltage on trace A and C and make trace B the ground. In this case the fast and slow axes will be 45 degrees from the X and Y axes. We measure the voltage needed to imitate a half wave-plate in the DC scenario. Figure 13(b) shows that the voltage needed for to emulate a half wave-plate is 18 V. Figure 13(c) shows the chip is wire-bonded to the PCB that provides the driving signals. For the DC signal it will see open circuit. However, RF signal coming in from the input side will be terminated by the AC-coupled termination at 50 ohms on the output side.

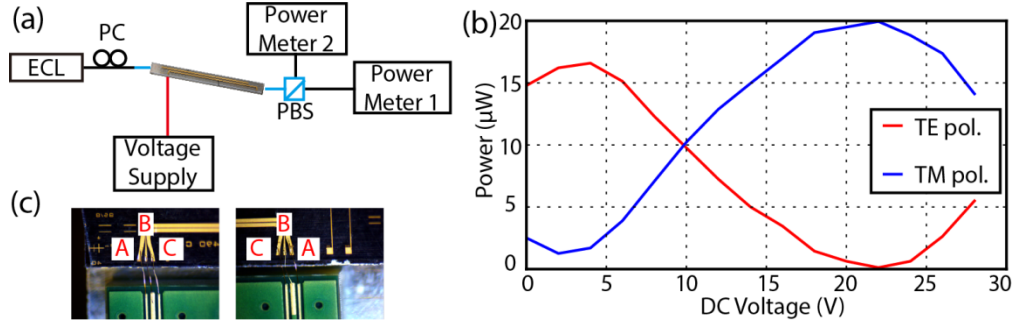


Figure 13 Polarization conversion by applying DC voltage. (a) *Experiment diagram.* ECL: external cavity laser; PC: polarization controller; PBS: polarization beam splitter. (b) *Power on TE and TM polarization vs. voltage measured by power meter 1 and power meter 2.* (c) *Electrode on chip wire-bonded to PCB. When we apply DC voltage, we apply the same voltage on A and C and ground B so that a vertical electrical field is built up in the waveguide region. The electrical traces work in traveling wave mode.*

II.2.b. Frequency Shifting Experiments

In the RF scenario, the amplitude of the vertical field equals the horizontal field. However, the amplitude ratio of the applied voltage would not remain one due to the difference in electrode distance, the interaction with the optical field, etc. We could adjust the amplitude ratio of the electrical field simply by tuning the phase delay between the signals applied on left and right electrodes.

Assume that the voltage on the left and right electrode is V_l and V_r ,

$$V_l = V_c \sin(\omega t) + V_d \cos(\omega t)$$

$$V_r = V_c \sin(\omega t) - V_d \cos(\omega t)$$

where $V_c \sin(\omega t)$ is the common voltage that creates the vertical field, and $V_d \cos(\omega t)$ is the differential voltage that builds up the horizontal field. We can combine the two terms into one sinusoidal wave with a phase term φ ,

$$V_l = \sqrt{V_c^2 + V_d^2} \sin(\omega t + \varphi)$$

$$V_r = \sqrt{V_c^2 + V_d^2} \sin(\omega t - \varphi)$$

where

$$\varphi = \arctan(V_d / V_c)$$

The phase delay between the two signals is 2φ and the two signals have equal amplitude. We only need to adjust the phase delay of the two signals to change the ratio of the vertical and horizontal fields and maintain their same amplitude.

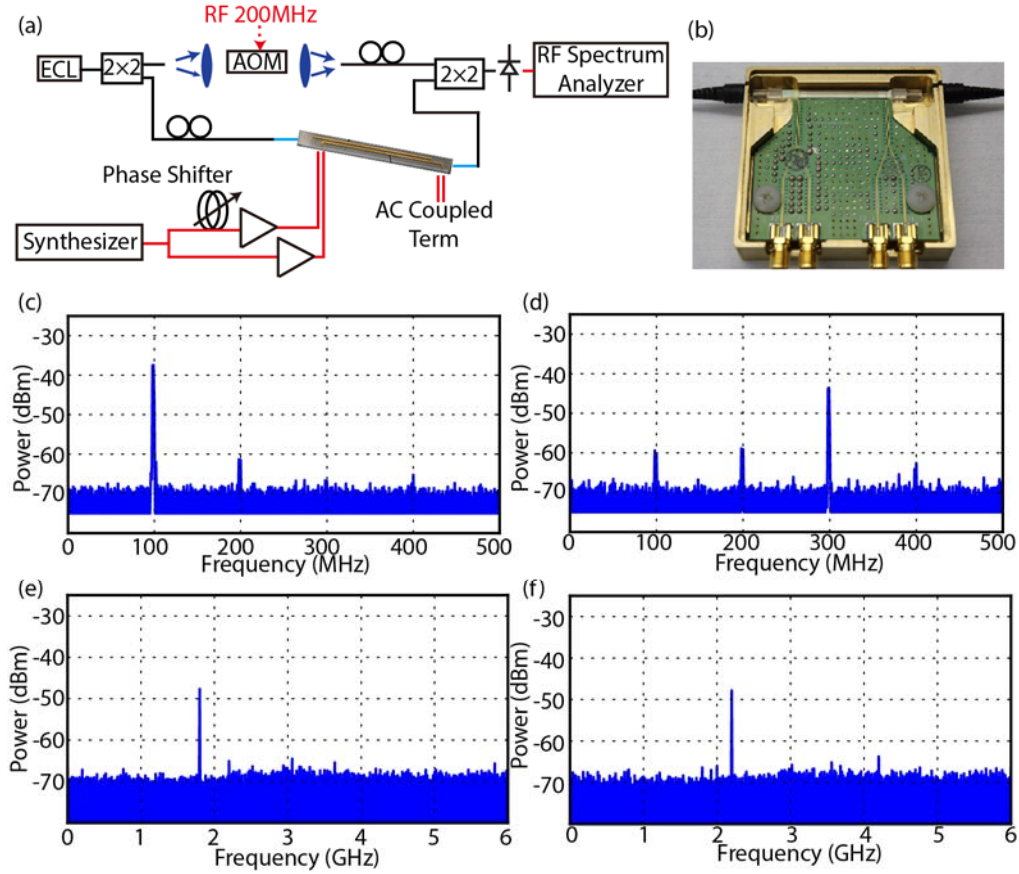


Figure 14 RF measurement. (a) Experiment diagram. AOM: acoustic optical modulator. (b) Integrated chip with PCB driving circuit. (c-d) Frequency down/up conversion at 100 MHz. (e-f) Frequency down/up conversion at 2 GHz.

We use the heterodyne detection to see DC tone, up and down conversion frequency tones simultaneously. An acoustic optical modulator on the reference arm shifts the DC tone to 200 MHz in Figure 14 (a), and on the signal arm, the light co-propagate with the electrical field in the device and therefore is modulated to a new frequency at the output. The synthesizer feeds two RF amplifiers that increase the power to 30 dBm to modulate the light. A phase shifter adjusts the phase delay between the two electrical signals. The phase delay is critical because it corresponds to the amplitude of the electrical field in the vertical and horizontal direction. The RF spectrum analyzer presents the intensity of the spectrum. It will fold the "negative" frequency to the "positive", so in the case where we modulate at 2 GHz, will we see that the -1st order tone at -1.8 GHz is folded to +1.8 GHz and +1st order tone still stays at 2.2 GHz. Figure 14 (b) shows integrated LiNbO₃ device wire-bonded with PCB and interfaced with a pair of polarization maintaining (PM) fibers. Figure 14 (c-d) shows frequency down/up conversion at 100 MHz. The DC tone for the down conversion is suppressed at 23 dB below the major -1st order tone for the down conversion and the -1st tone and DC tone are suppressed more than 15 dB below the major +1st order frequency tone for the up conversion. Figure 14 (e-f) shows frequency down/up conversion at 2 GHz. In both up/down conversion we achieve extinction ratio better than 20 dB.

II.2.c. Optical isolation experiment

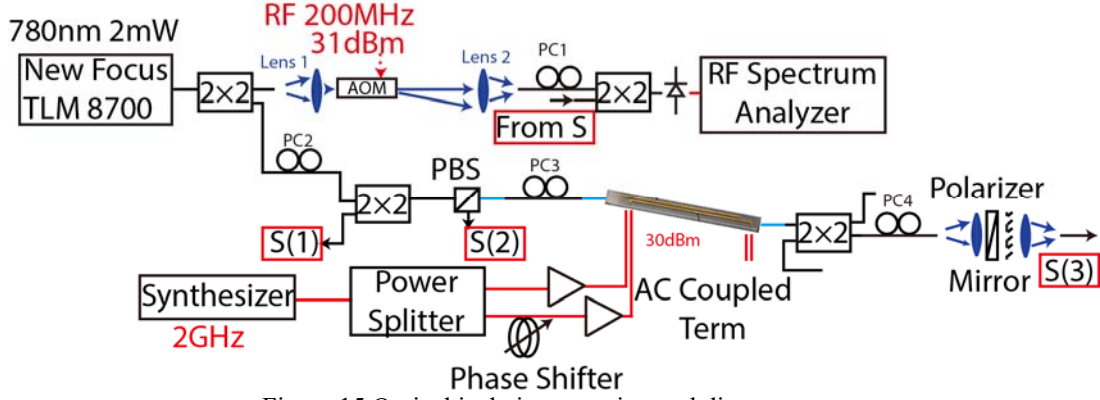


Figure 15 Optical isolation experimental diagram.

Figure 15 shows the diagram for optical isolation characterization. The laser is split onto reference arm and signal arm by a 50/50 splitter. The light on the reference arm is shifted by the AOM by 200 MHz. The light on the signal arm first goes through a 50/50 splitter used as an optical circulator. Then it goes through a PBS to make sure only TE polarization light goes through. The PC3 and the PM fiber input imitates a QWP and make sure that the input into the LiNbO₃ chip is a circularly polarized light. The 2 GHz electrical sinusoidal in-phase and quadrature phase signals drive and co-propagate with the lightwave to yield frequency shift and polarization conversion at the output of the chip. The PM fiber, 50/50 splitter and PC4 imitates a QWP to convert the circularly polarized light at the output to a linear polarized light. The PC3 and PC1 is optimized such that the light right after PC4 beats with the reference and generates the single tone frequency shift. Then we adjust PC4 to align the output to the linear polarizer. At S(3) the signal mixes with the reference and we verify it is still a single tone frequency generation. We present the forward transmission results in Figure 16.

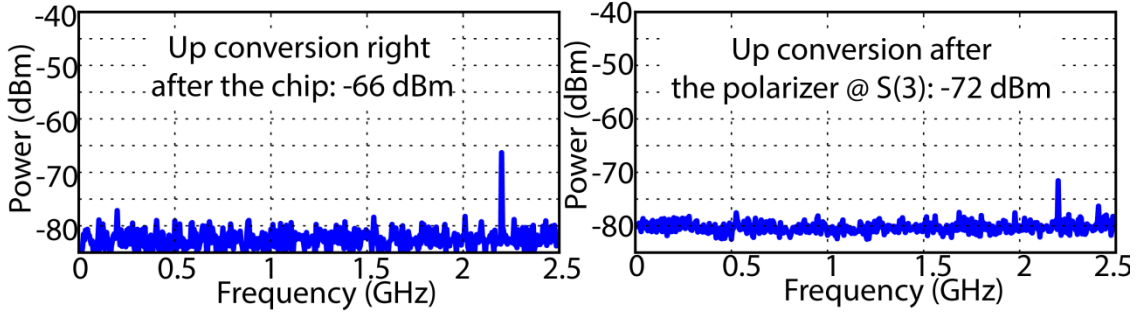


Figure 16 Single frequency tone conversion, forward transmission.

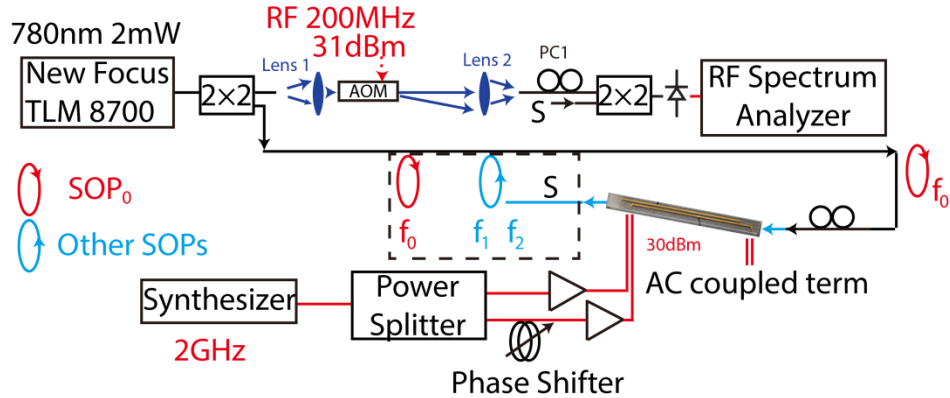


Figure 17 Optical isolation, backward transmission.

In Figure 17 we generate an equivalent light of frequency shifter output and send light backward while we are modulating the chip in the forward configuration. The light after backward transmission has two parts: polarization converted part (f_1 , f_2) and polarization unconverted part (f_0). However, the unconverted part f_0 will be blocked by the polarizer, f_1 and f_2 will go through polarizer. And we can determine the isolation suppression by measuring the polarization converted light and original reflected light by adjusting PC on the reference arm (PC1).

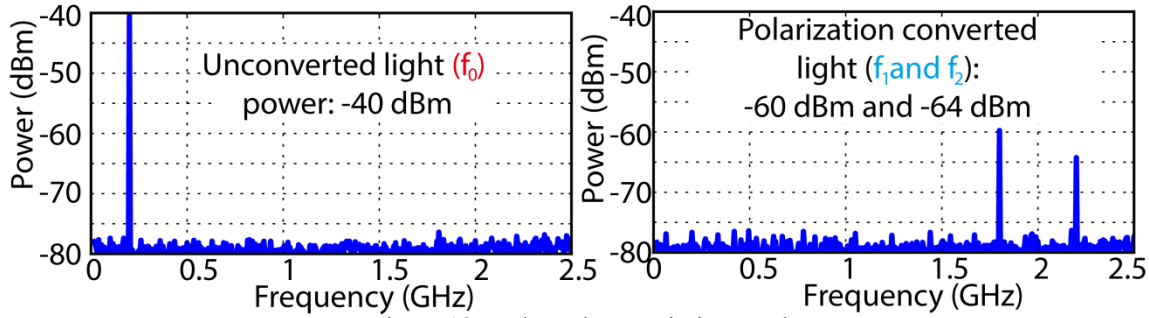


Figure 18 Backward transmission results.

The f_0 is the unconverted frequency component while we transmit light backward. Because the modulation signal no longer co-propagate with the optical lightwave, the modulation would not be applied onto the optical waves. Figure 18 shows that the unconverted part f_0 is -40dBm and remains the same frequency and polarization as the output. The unconverted component will be isolated by the polarizer on the input side. On the right figure, the converted power at f_1 and f_2 is -60 dBm and -64 dBm for the -1st and +1st order frequency tone. The isolation is 18.5 dB comparing the unconverted tone f_0 and converted f_1 and f_2 .

II.2.d. Theory and experiment on using larger electro-optical coefficient (r_{33} and r_{42})

For the current chip under testing we are using the smallest electro-optical coefficient in the lithium niobate chip. This choice requires a very large RF power or a very long waveguide to realize the function of a half wave plate. We came up with a new orientation and found that we could use larger coefficients for the frequency shifting application. Instead of using an x-cut LiNbO₃ device and z propagation, we propose to use an x cut device in y propagation.

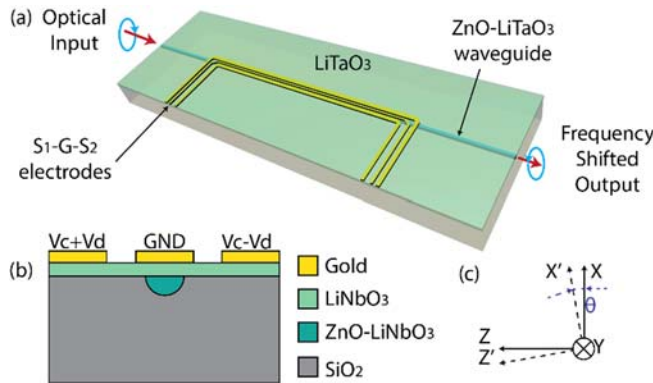


Figure 19 (a) Device schematic. (b) Device cross-section and rotation of index ellipsoid for the X-cut, Y-propagating LiTaO₃ device with applied common and differential voltages to the electrodes.

When E_x and E_y fields are present, we have the ellipsoid equation as

$$x^2 \left(\frac{1}{n_o^2} + r_{13} E_z \right) + z^2 \left(\frac{1}{n_e^2} + r_{33} E_z \right) + 2r_{42} E_x xz = 1$$

Let us assume the axis rotate along y axis by θ degree

$$\begin{aligned} x &= x' \cos(\theta) - z' \sin(\theta) \\ y &= y' \\ z &= x' \sin(\theta) + z' \cos(\theta) \end{aligned}$$

We plug in the new axis into the ellipsoid equation and get

$$\begin{aligned} &x'^2 \left(\cos^2 \theta \left(\frac{1}{n_o^2} + r_{13} E_z \right) + \sin^2 \theta \left(\frac{1}{n_e^2} + r_{33} E_z \right) + \sin 2\theta r_{42} E_x \right) \\ &+ z'^2 \left(\sin^2 \theta \left(\frac{1}{n_o^2} + r_{13} E_z \right) + \cos^2 \theta \left(\frac{1}{n_e^2} + r_{33} E_z \right) - \sin 2\theta r_{42} E_x \right) \\ &+ x' z' \left(-\sin 2\theta \left(\frac{1}{n_o^2} + r_{13} E_z \right) + \sin 2\theta \left(\frac{1}{n_e^2} + r_{33} E_z \right) + \cos 2\theta r_{42} E_x \right) = 1 \end{aligned}$$

We want to make the cross term equal to zero.

$$\left(-\sin 2\theta \left(\frac{1}{n_o^2} + r_{13} E_z \right) + \sin 2\theta \left(\frac{1}{n_e^2} + r_{33} E_z \right) + \cos 2\theta r_{42} E_x \right) = 0$$

Note that we make a big assumption here that we are able to eliminate the birefringence between n_o and n_e . Therefore we have

$$\begin{aligned} \sin 2\theta (r_{33} - r_{13}) E_z + \cos 2\theta 2r_{42} E_x &= 0 \\ \frac{E_z}{E_x} &= \frac{2r_{42} \cos 2\theta}{(r_{13} - r_{33}) \sin 2\theta} \end{aligned}$$

For the same device length, the voltage needed to achieve a half wave plate is reduced by 2.85 times by utilizing much larger electro-optical coefficients r_{33} and r_{42} .

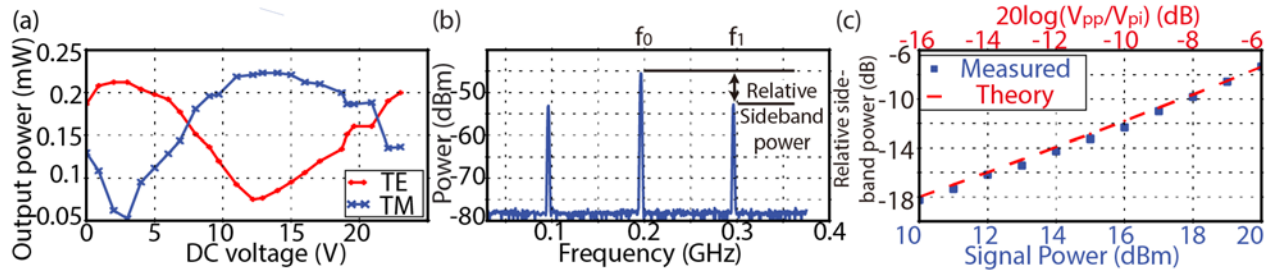


Figure 20(a) TE - TM conversion by applying DC voltage. (b) Spectrum for phase modulation from a sinusoidal driving signal at 20dBm. (c) Measured and theory relative sideband power vs. phase modulation power.

Figure 20(a) shows the characterization of the polarization conversion by applying a differential voltage to the two outer electrodes, creating a lateral field to change the birefringence. The input light is linearly polarized, 45° to both X- and Z- axes and the power on transverse electric (TE) and transverse magnetic (TM) polarizations is monitored. The voltage to convert the TE to TM is 10 V. Figure 20(b) shows the phase modulation spectrum by using heterodyne detection with an acoustic optical modulator (AOM) at 200 MHz when the RF driving signal is a 100 MHz, 20 dBm sinusoidal wave. We apply the RF signal on the Z axis and launch a linearly polarized

input light with field parallel to the Z axis. Figure 20(c) shows the measurement of the power difference between DC at 200 MHz and first order tone at 300 MHz when RF driving power varies from 10 - 20 dBm (blue cross). For comparison, Figure 20(c) also shows the theory curve of relative first-order sideband power vs. $(V_{p-p}/V_{\pi})^2$ (dashed red) on a typical phase modulator. The output of a phase modulator is $\exp[jV_{p-p}/(2V_{\pi})\sin(\omega_0 t)]$. When the signal power is 20 dBm or 6.3 V peak to peak for sine wave with 50 Ω load resistance, our measurement shows the same relative sideband power (-7.3 dB) when $20\log_{10}(V_{p-p}/V_{\pi}) = -6$ dB, or $V_{p-p} = 0.5 V_{\pi}$. Therefore, the V_{π} for the device as a phase modulator is 12.6 V at 100 MHz for an RF signal on the lateral/Z axis.

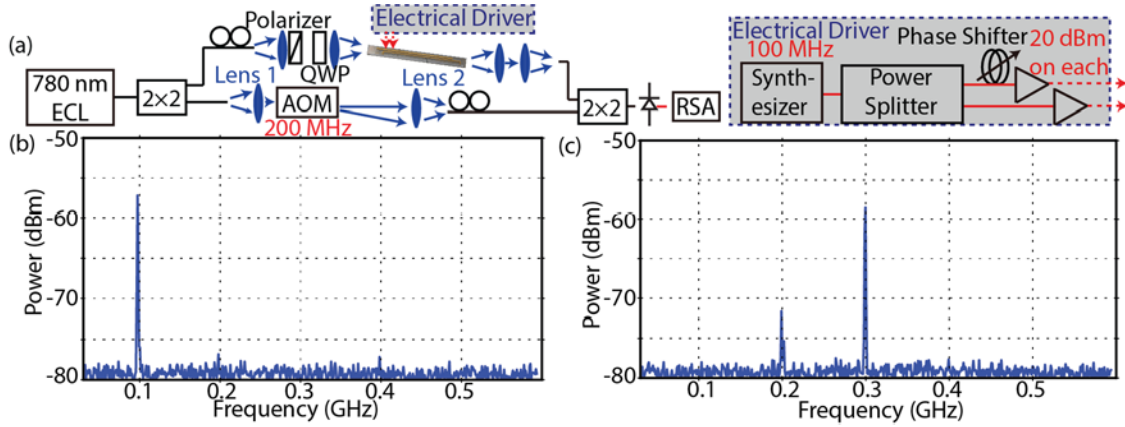


Figure 21(a) Experimental diagram using heterodyne detection. (b) 100 MHz up-conversion, 20 dB side lobe suppression. (c) 100 MHz down-conversion, 14 dB side lobe suppression.

Figure 21(a) shows the experimental setup that employs heterodyne detection to resolve DC, down conversion and up conversion frequency tones. This setup involves an external cavity laser (ECL) at 780 nm wavelength and an AOM on the reference arm that shifts the optical frequency to 200 MHz. On the signal arm, the device converts the input light to a circular polarization with a polarization controller (PC), a polarizer and a quarter wave plate (QWP). We use a synthesizer, a power splitter, and two RF amplifiers to generate, split and amplify a 100 MHz sinusoidal wave. By adjusting the phase delay between two electrical signals, the phase shifter controls the power ratio between the vertical and lateral field to fulfill the certain ratio. We mix the reference and signal in a 50/50 splitter and receive the beat with a photo-diode and display the frequency information on an RF spectrum analyzer (RSA). The PC on the reference arm aims to align the reference polarization with the signal polarization.

The down-conversion tone in Figure 21(b) shows up at 100 MHz, and the side lobe suppression is 20 dB with -12 dB conversion efficiency (CE). Figure 21(c) shows the up-conversion, and the frequency tone is at 300 MHz with a suppression of 14 dB and -13 dB CE. 40 V DC voltage across the lateral/Z axis is applied to null the intrinsic birefringence. The RF power on each arm is 20 dBm, making it a total of 23 dBm RF power consumption. It is a 10 dB improvement compared to 33dBm RF power in [3]. The power consumption is determined by a few factors. 1) Device active length affects the modulation length. 2) Operation wavelength determines how fast the phase changes. 3) Electrode gap/ electrode design impacts the overlap integral between the electrical field and the optical field. 4) Modulation frequency affects the RF loss and how much electrical power can interact with optical light. 5) Material decides the strength of the electro-optical coefficients for the modulation to utilize. The material also determines the intrinsic birefringence

and how much DC bias voltage is needed to null it. It is possible to obtain zero birefringence by adjusting Nb/Ta ratio in the $\text{LiNb}_{1-x}\text{Ta}_x\text{O}_3$ material.

II.3. 780 nm Laser design, fabrication, and testing based on AlGaAs/GaAs Multiple Quantum Wells (MQWs) wafer stack

Based on an AlGaAs/GaAs MQWs wafer stack shown in Table 2 below, we are able to design an all-active (instead of active-passive) ring cavity laser with Multimode Interference (MMI) coupler lasing at 780 nm wavelength. This is an initial demonstration of the capability for 780 nm laser and a testing run based on low resolution contact aligner tool. In the next version of ring cavity laser, we plan to use new active-passive wafer stack, direct wafer bonding technology, and high resolution projection lithography tool (stepper). The reason of using MMI coupler for the low resolution run, is the limitation of minimum feature size of contact lithography tool of 1 μm , which is far beyond directional coupler working range for the design on the existing wafer stack at 780 nm wavelength.

Table 2 5-QW wafer stack with PL wavelength at 780 nm.

780 nm laser wafer stack			PL wavelength 763 nm		
p+ doped cap	GaAs	160nm	p-type	5.00E+19	Zn
Linearly Graded Region	GaAs to $\text{Al}_{0.8}\text{Ga}_{0.2}\text{As}$	10 nm	p-type	1.00E+18	C
p-doped upper cladding	$\text{Al}_{0.8}\text{Ga}_{0.2}\text{As}$	780 nm	p-type	1.00E+18	C
undoped core	$\text{Al}_{0.4}\text{Ga}_{0.6}\text{As}$	20nm	UID	0.00E+00	UID
QW (1)	GaAs	2.8 nm	UID	0.00E+00	UID
Barrier	$\text{Al}_{0.4}\text{Ga}_{0.6}\text{As}$	7nm	UID	0.00E+00	UID
QW (2)	GaAs	2.8 nm	UID	0.00E+00	UID
Barrier	$\text{Al}_{0.4}\text{Ga}_{0.6}\text{As}$	7nm	UID	0.00E+00	UID
QW (3)	GaAs	2.8 nm	UID	0.00E+00	UID
Barrier	$\text{Al}_{0.4}\text{Ga}_{0.6}\text{As}$	7nm	UID	0.00E+00	UID
QW (4)	GaAs	2.8 nm	UID	0.00E+00	UID
Barrier	$\text{Al}_{0.4}\text{Ga}_{0.6}\text{As}$	7nm	UID	0.00E+00	UID
QW (5)	GaAs	2.8 nm	UID	0.00E+00	UID
undoped core	$\text{Al}_{0.4}\text{Ga}_{0.6}\text{As}$	300nm	UID	0.00E+00	UID
n-type lower cladding	$\text{Al}_{0.8}\text{Ga}_{0.2}\text{As}$	1100 nm	n-type	1.50E+18	Si
Linearly Graded Region	$\text{Al}_{0.8}\text{Ga}_{0.2}\text{As}$ to GaAs	10 nm	n-type	1.50E+18	Si
Buffer Layer Growth	GaAs	100 nm	n-type	1.50E+18	Si
n-type substrate	GaAs	675 micron	n-type	1.00E+18	Si

II.3.a. Design and Simulation of MMI coupler based on MQWs wafer stack (all-active)

We simulate the band diagrams of the existing MQWs wafer stack shown in Table 2. There are five quantum wells in this wafer stack. In Figure 22, with applying bias voltage, the Fermi level for electrons rises into the wells where electrons accumulate and forms stimulated radiation.

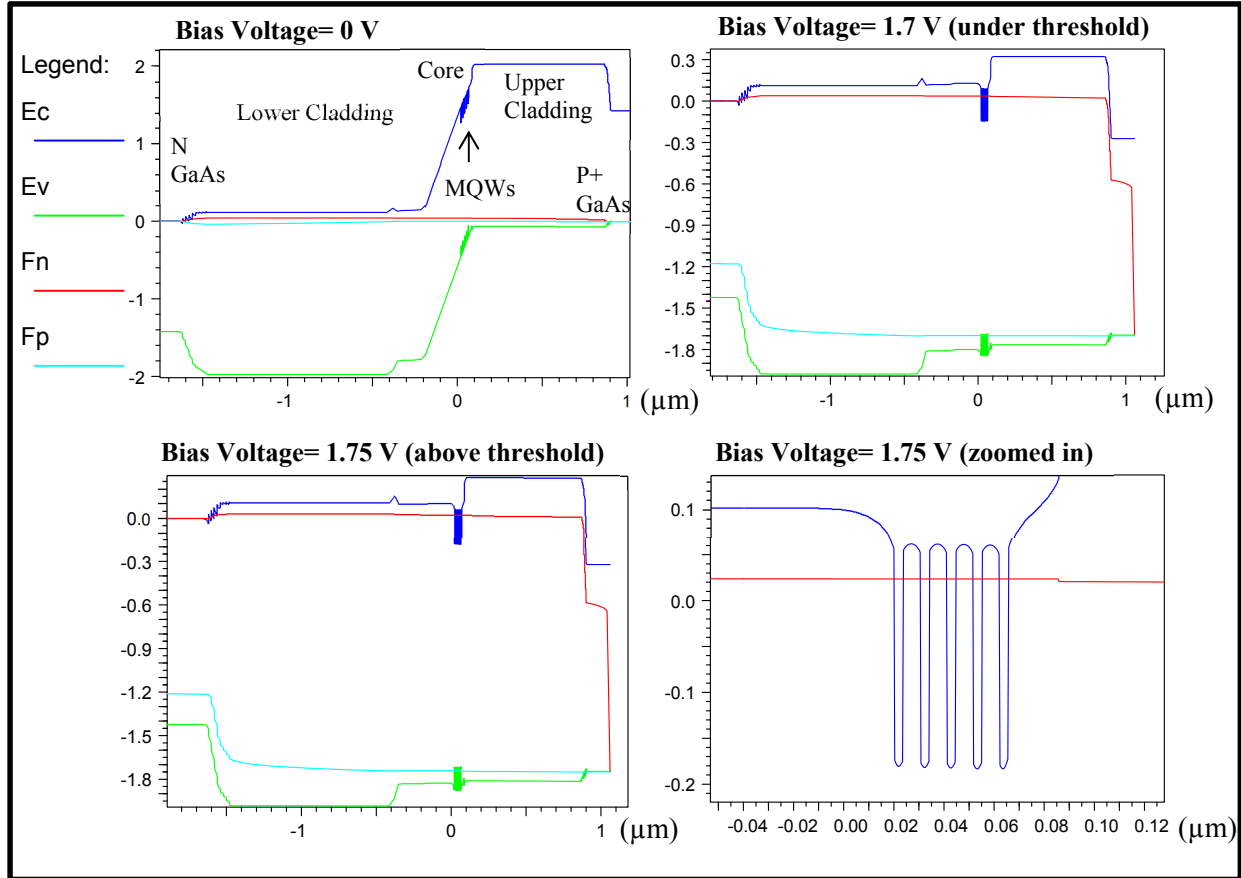


Figure 22 Band diagrams of GaAs/AlGaAs MQWs laser stack (all-active) with Bias voltage of 0 V, 1.7 V, and 1.75V.

Based on the existing MQWs wafer stack, we simulate MMI couplers at 780 nm wavelength. As shown in Figure 23, a 1x2 MMI with 50:50 splitting ratio is simulated. The designed dimension is $10 \times 225 \mu\text{m}^2$, which is limited by the minimum feature size of contact lithography tool, because the waveguide width and waveguide separation can not shrink down below $1 \mu\text{m}$. Therefore, the width of MMI coupler is scaled up to about $10 \mu\text{m}$ and then $200\text{-}650 \mu\text{m}$ for length. In addition, we simulated 2x2 MMI couplers with power splitting ratio at 50:50 and 80:15, as shown in Figure 24 and Figure 25, respectively.

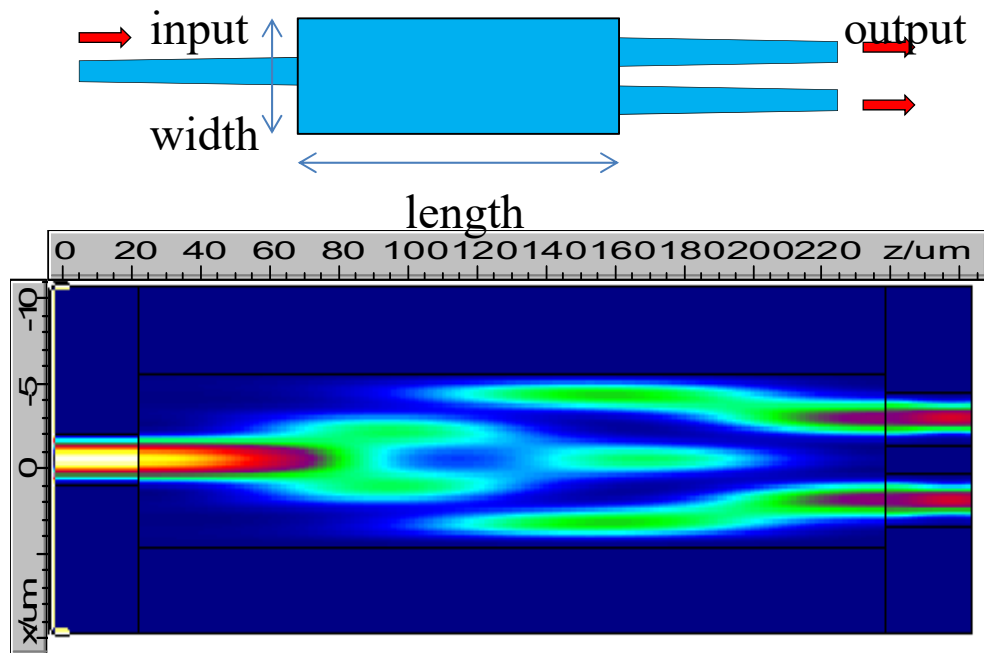


Figure 23 Simulated 1x2 MMI coupler based on MQWs wafer stack (all-active) at 780 nm wavelength. The designed MMI width is 10 μm ; length is 225 μm ; two output arms are off-set from center by 2.35 μm .

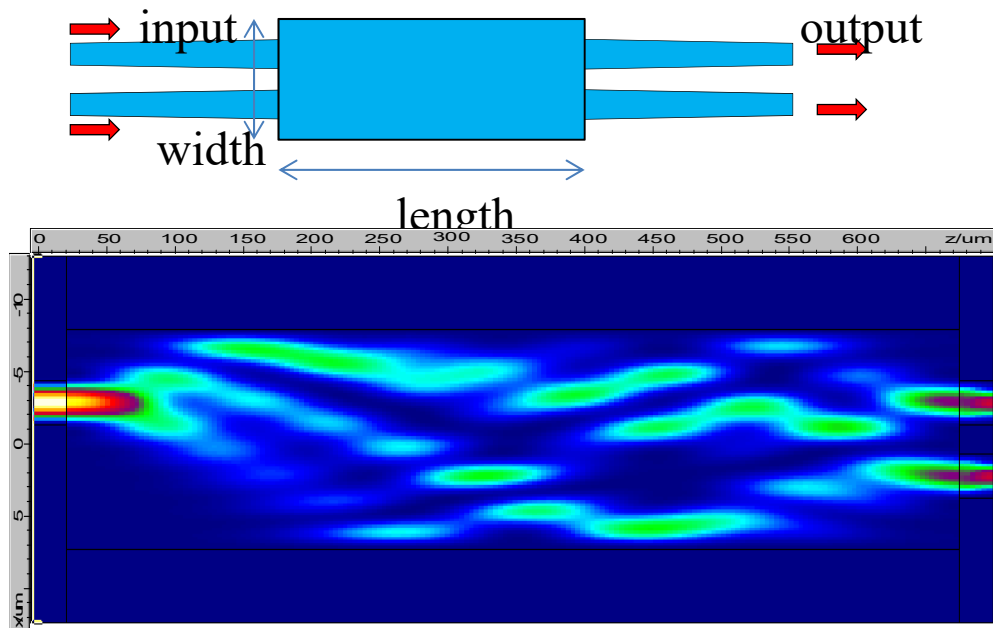


Figure 24 Simulated 2x2 MMI coupler based on MQWs wafer stack (all-active) at 780 nm wavelength. The designed MMI width is 15 μm ; length is 650 μm ; two output arms are off-set from center by 2.5 μm ; designed splitting ratio is 50:50.

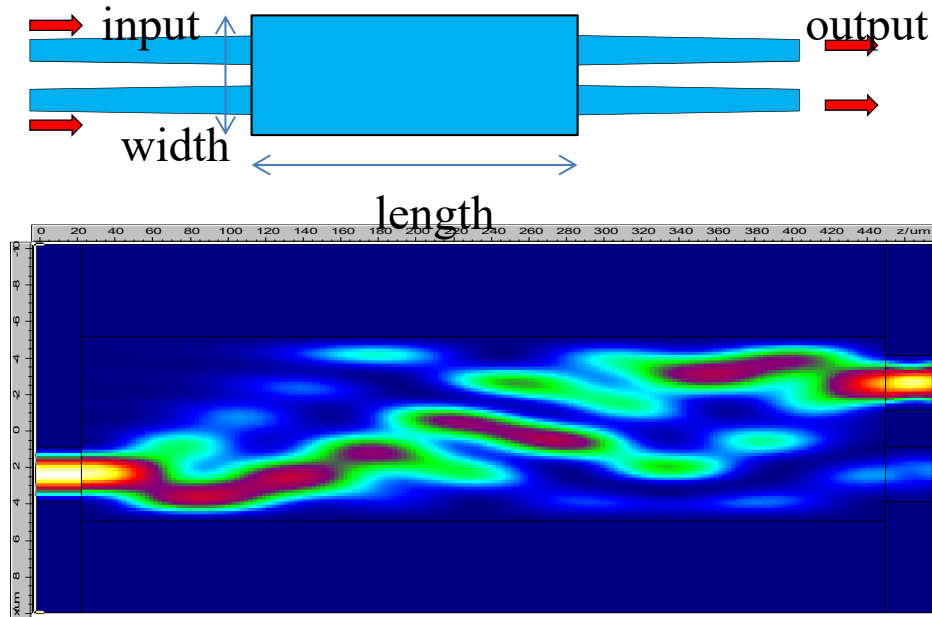


Figure 25 Simulated 2x2 MMI coupler based on MQWs wafer stack (all-active) at 780 nm wavelength. The designed MMI width is 10 μm ; length is 425 μm ; two output arms are off-set from center by 2.5 μm ; designed splitting ratio is 80:15.

We designed ring cavity lasers with simulated MMI couplers. A simple design of ring cavity laser with MMI coupler is shown in Figure 26. In this design, the MMI coupler has strong compatibility regarding to fabrication tolerance, but theoretically introduces 3 dB round trip extra coupling loss. The bending radius is varied from 50 μm to 300 μm . Waveguide width is 3 μm due to lithography limitation, which has few modes existing instead of single mode.

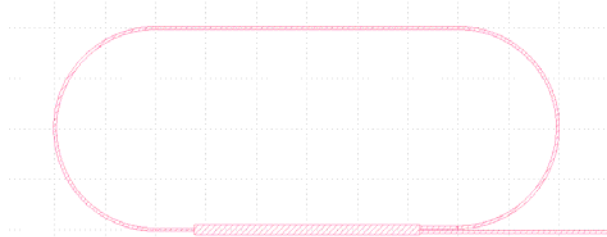


Figure 26 Design of ring cavity laser with 1x2 MMI coupler

Figure 27 is a ring cavity laser with with 2x2 MMI coupler.

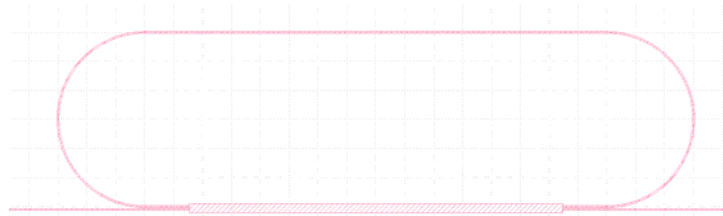


Figure 27 design of ring cavity laser with 2x2 MMI coupler.

To select lasing wavelength, we also designed double-ring cavity with 2x2 MMI couplers, as shown in Figure 28 and Figure 29. The two cavities have slightly different free spectral range (FSR). Using Vernier effect, a single lasing wavelength can be selected.

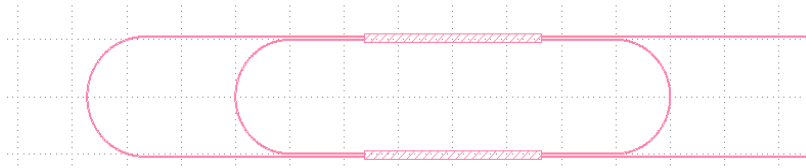


Figure 28 Design of double-ring cavity laser with 2x2 MMI couplers.

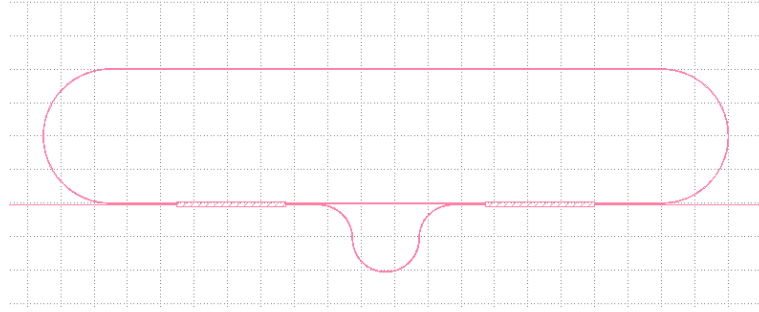


Figure 29 Design of double-ring cavity laser with 2x2 MMI couplers

Figure 30 shows the layout of laser devices. Basically we designed the device with simulated parameters, and varying each parameter with expectation of performance variation due to low resolution lithography tool and etching condition.

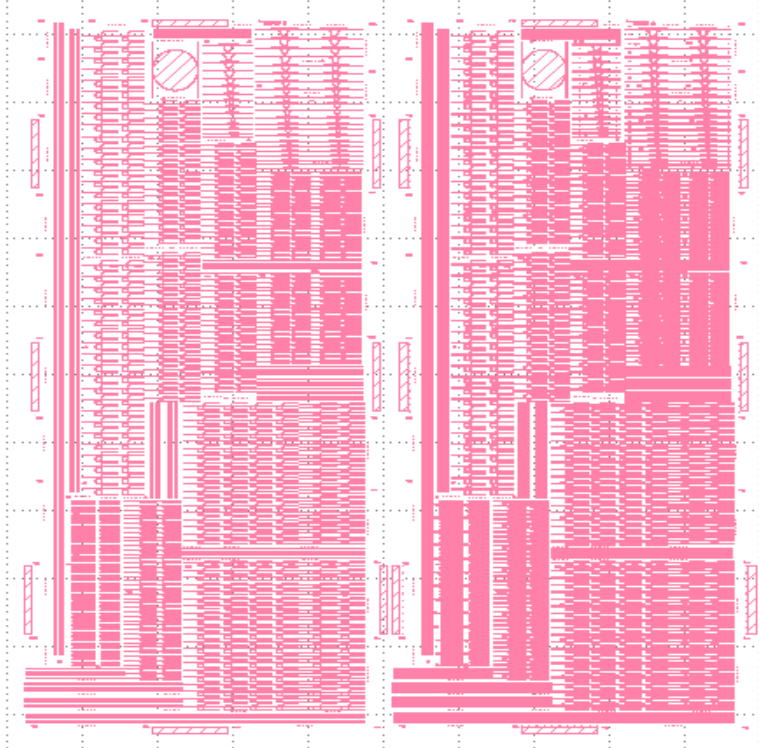


Figure 30 Layout of designed ring cavity laser with MMI couplers.

II.3.b. Fabrication of Ring cavity laser with MMI couplers

We fabricated all-active ring cavity laser using MQWs wafer in Table 2. We start with initial wafer cleaning. Lithography tool we used is Karl Suss contact aligner. We define the waveguide by Cl_2/BCl_3 dry etching in an ICP chamber. The waveguide core is fully etched. Afterwards, 150 nm PECVD SiO_2 deposit on etched waveguide as isolation layer. Then we use coat BCB to

planarize the wafer, followed by CF_4/O_2 RIE dry etching until the exposure of waveguide top surface. BOE release for 1 min helps to remove the isolation layer above P-contact area. Finally, we do Pt/Ti/Pt/Au metal contact evaporation, lift-off, and rapid thermal annealing at 380 °C for 30 seconds. Figure 32 shows the photos of double-ring cavity laser.

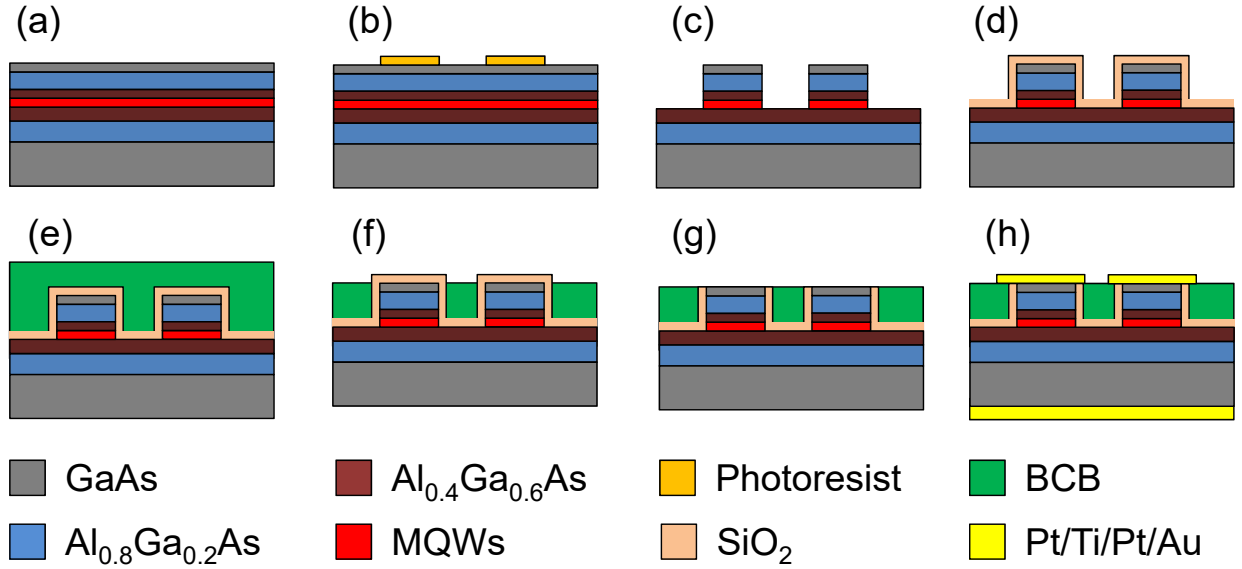


Figure 31 Fabrication flow chart (a) initial MQWs wafer and cleaning; (b) Photo lithography; (c) Cl_2/BCl_3 ICP dry etching; (d) PECVD SiO_2 deposition; (e) BCB spinning; (f) CF_4/O_2 RIE dry etching; (g) BOE release SiO_2 ; (h) P-contact and N-contact metal lift-off.

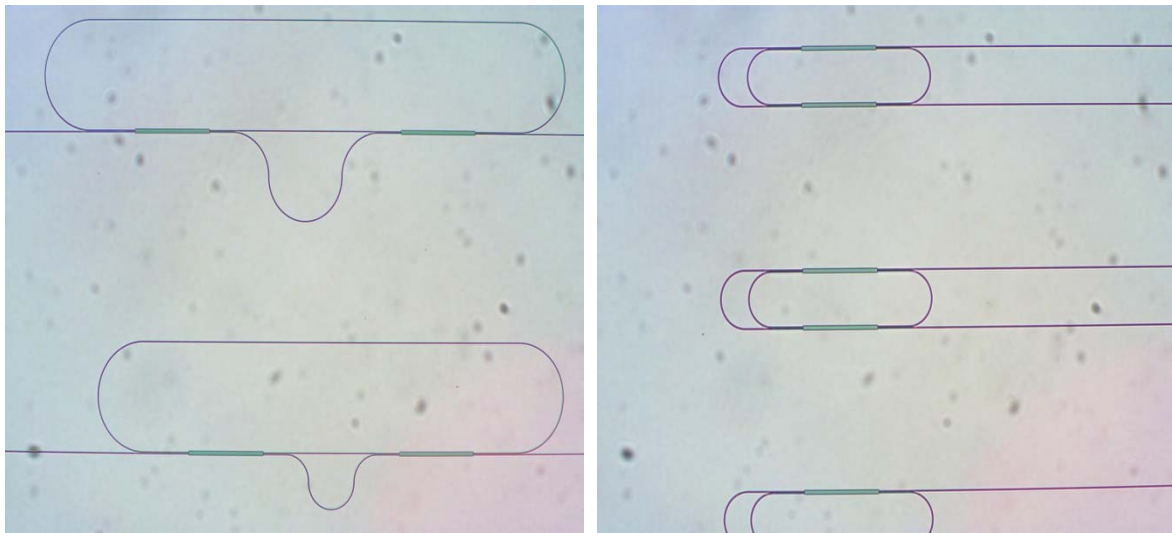


Figure 32 Device photos of double-ring cavity laser with MMI couplers.

II.3.c. Testing results of ring cavity laser

Figure 33 and Figure 34 are the I-V curve and $\text{IdV}/\text{dI-I}$ curve of ring cavity laser. Figure 35 and Figure 36 are spectrum and L-I curve of ring cavity laser. The driving current is in CW mode. The measured device is in a ring cavity with a 1x2 MMI coupler. The bending radius of the

ring cavity is 100 μm . The lasing wavelength is at 787 nm, which is red drift from PL wavelength. To test the dependence of lasing wavelength, we also tested the ring cavity laser with pulsed driving current, as shown in Figure 37, where the lasing wavelength 773 nm. Therefore, we expect an influence on lasing wavelength from heating issue. In addition, we tested straight cavity FP laser, which we used to calibrate PL wavelength. As a result shown in Figure 38, the lasing wavelength is matched well with our previous calibration for PL wavelength at 780 nm. All the pulsed current has 1 % duty cycle and 0.1 μs duration.

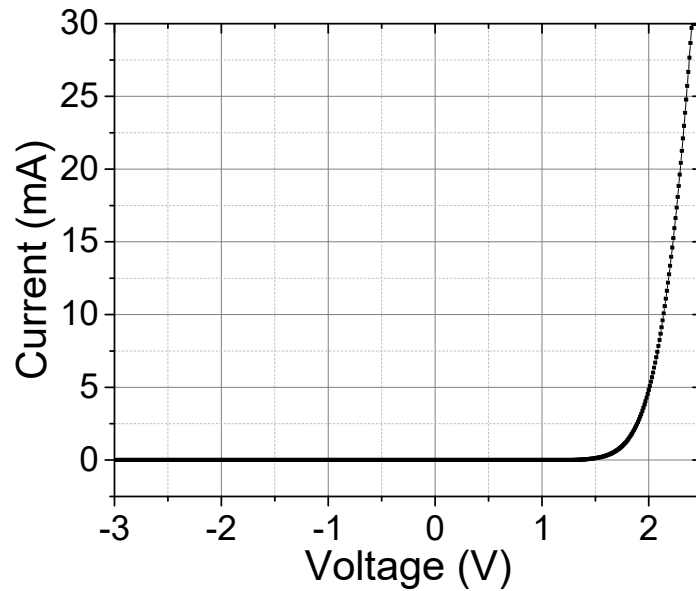


Figure 33 I-V curve of ring cavity laser.

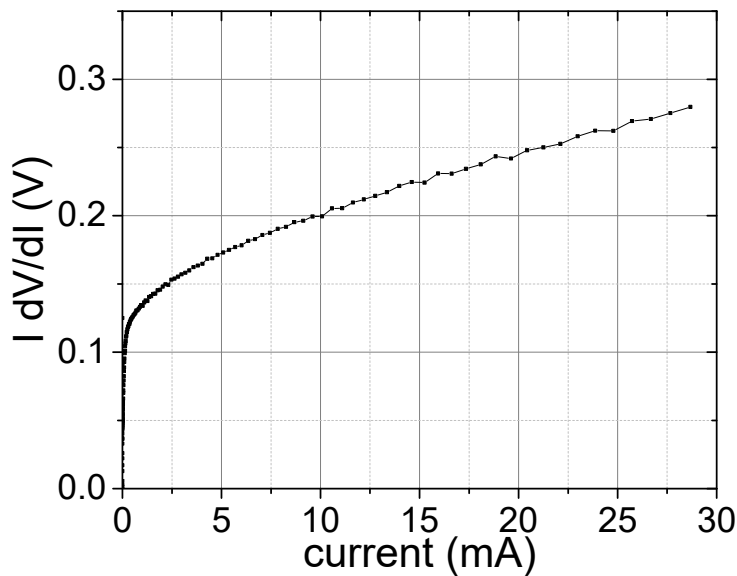


Figure 34 $I \frac{dV}{dI}$ -I curve of ring cavity laser.

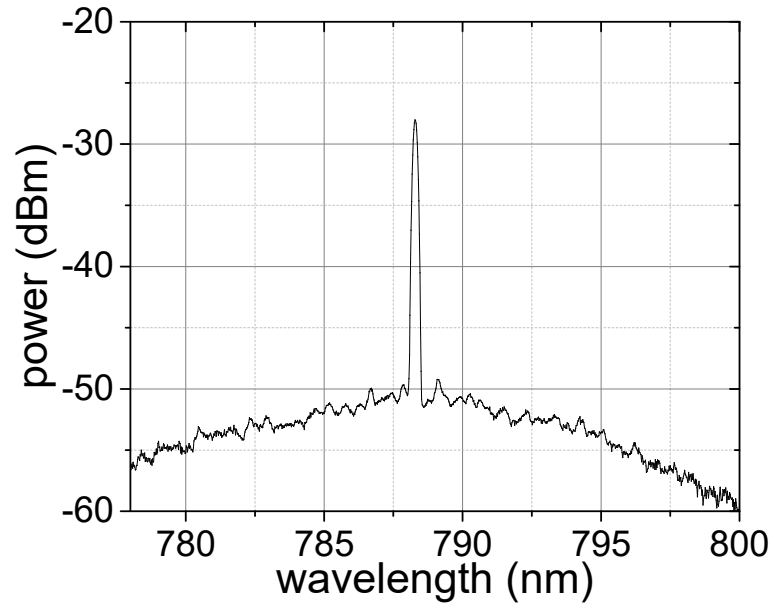


Figure 35 spectrum of ring cavity laser with driving current in CW mode.

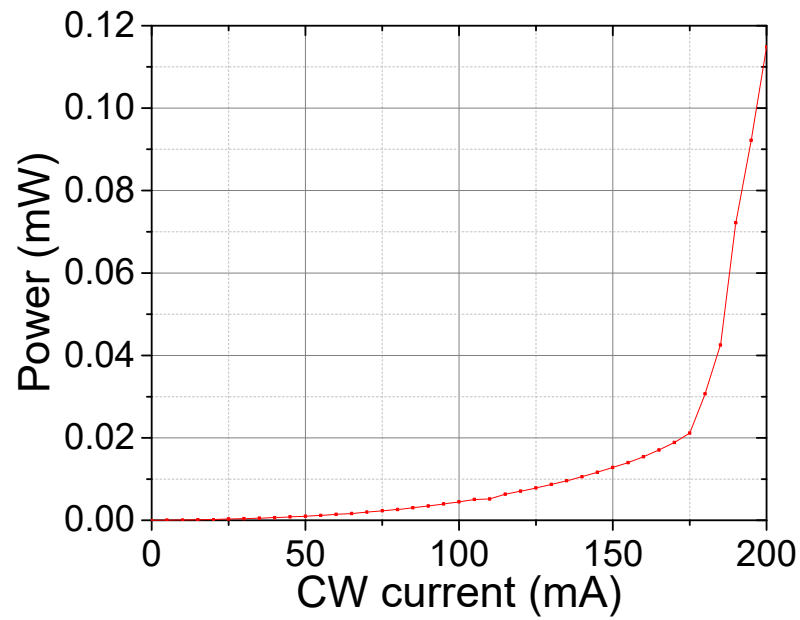


Figure 36 L-I curve of ring cavity laser.

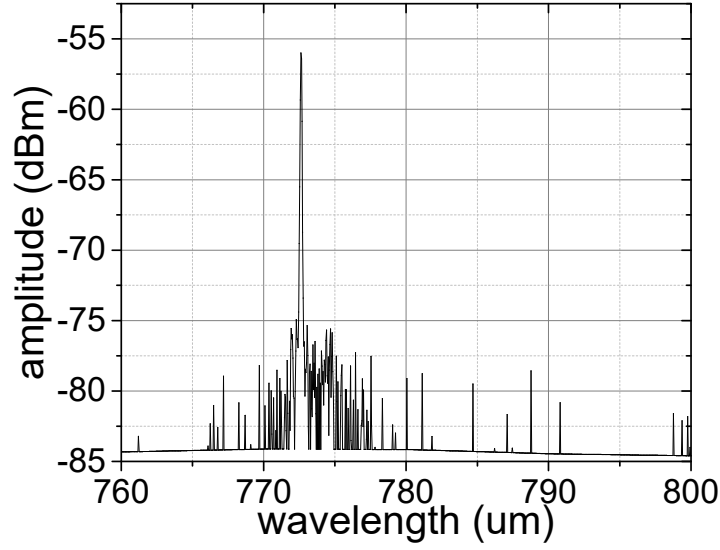


Figure 37 Spectrum of ring cavity laser with pulsed driving current.

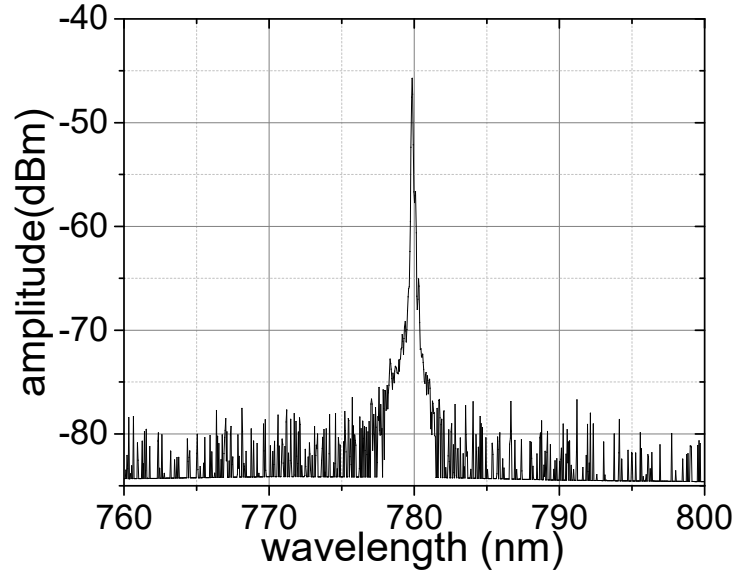


Figure 38 Spectrum of straight cavity FP laser with pulsed driving current.

II.4. Design and simulation of active-passive integrated ring cavity laser

In this section, we are going to design AlGaAs MQWs ring cavity laser based on active-passive integration. There are two designs between AlGaAs platform and AlGaAs/Si₃N₄ bonding platform. AlGaAs platform has strong compatibility with active-passive integration, but might introduce additional propagation loss from passive AlGaAs waveguide due to MQWs removal. AlGaAs/Si₃N₄ bonding platform combines AlGaAs MQWs and low loss Si₃N₄ waveguide, but needs to achieve low loss interconnect between materials with bonding technology.

II.4.a. AlGaAs MQWs design and simulation

Figure 39 indicates the band diagrams of AlGaAs MQWs laser stack for active-passive integration. The well is $\text{Al}_{0.1}\text{Ga}_{0.9}\text{As}$ and barrier is $\text{Al}_{0.3}\text{Ga}_{0.7}\text{As}$. Well thickness is 7 nm and barrier thickness is 5 nm. There are 50 nm $\text{Al}_{0.3}\text{Ga}_{0.7}\text{As}$ SCH layer on both sides of MQWs. Figure 40 and Figure 41 show the simulated PL wavelength and material gain with varying temperature. Figure 42 is the simulated I-V curve and L-I curve of the proposed AlGaAs MQWs stack based on a straight cavity FP laser.

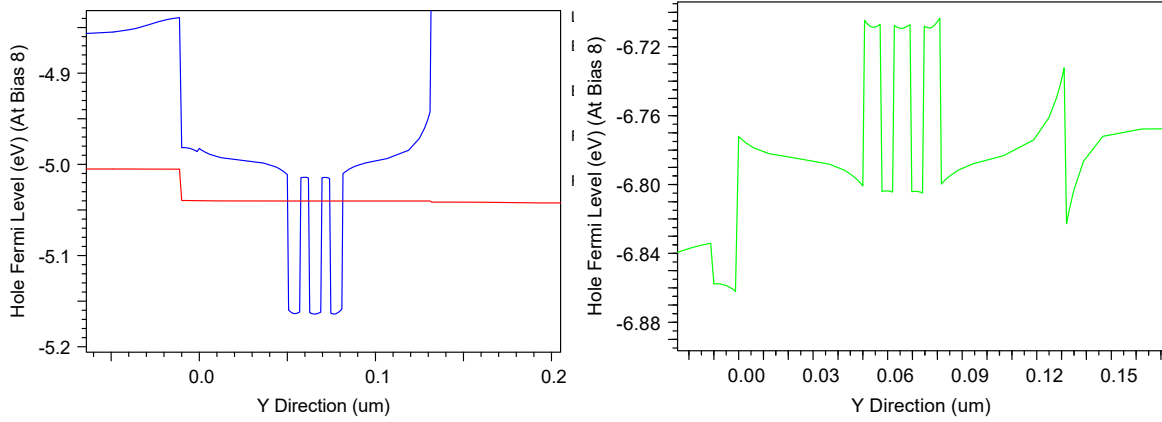


Figure 39 Band diagrams of AlGaAs MQWs laser stack for active-passive integration.

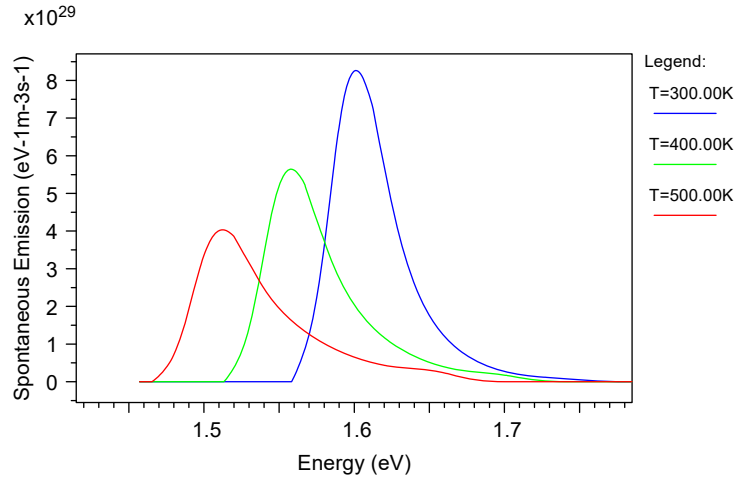


Figure 40 PL wavelength simulation of the proposed MQWs at 300 K (blue), 400 K (green), 500 K (red).

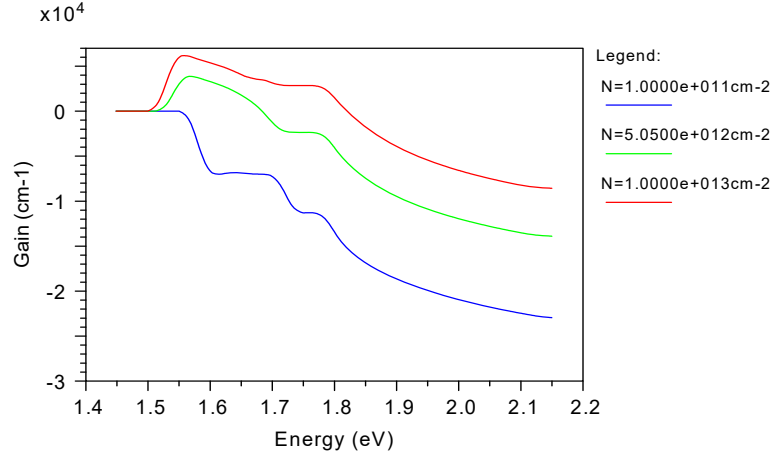


Figure 41 Simulated material gain of the proposed MQWs at 300 K (blue), 400 K (green), 500 K (red).
Light & Voltage vs Current

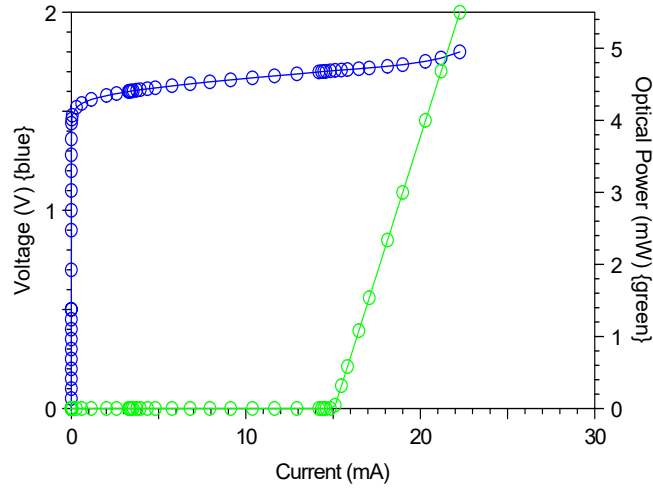


Figure 42 Simulated I-V and L-I curve based on a straight cavity FP laser.

II.4.b. AlGaAs platform ring cavity laser active-passive integration

Table 3 indicates the wafer stack proposed for AlGaAs active-passive integration. Basically, the MQWs are $\text{Al}_{0.1}\text{Ga}_{0.9}\text{As}/\text{Al}_{0.3}\text{Ga}_{0.7}\text{As}$ as simulated above. Waveguide core is 450 nm $\text{Al}_{0.5}\text{Ga}_{0.5}\text{As}$, which is separated from MQWs by 20 nm $\text{In}_{0.5}\text{Ga}_{0.5}\text{P}$ etch-stop layer for active-layer removal. There is about 1 μm $\text{Al}_{0.8}\text{Ga}_{0.2}\text{As}$ p-cladding and n-cladding. The whole wafer stack is upside down for wafer bonding.

Table 3 AlGaAs MQWs wafer stack for active-passive integration.

design 2a 780nm AlGaAs laser design with etch stop					
780 nm laser design					
n-contact	GaAs	300nm	n-type	3.00E+18	n-Si
Linearly Graded Region	$\text{Al}_{0.8}\text{Ga}_{0.2}\text{As}$ to $\text{Al}_{0.1}\text{Ga}_{0.9}\text{As}$	100 nm	n-type	3.00E+18	n-Si
n-type lower cladding	$\text{Al}_{0.8}\text{Ga}_{0.2}\text{As}$	900nm	n-type	1.50E+18	n-Si
Linearly Graded Region	$\text{Al}_{0.5}\text{Ga}_{0.5}\text{As}$ to $\text{Al}_{0.8}\text{Ga}_{0.2}\text{As}$	25 nm	n-type	5.00E+16	n-Si
lightly n-doped core	$\text{Al}_{0.5}\text{Ga}_{0.5}\text{As}$	400nm	n-type	5.00E+16	n-Si
Linearly Graded core	$\text{Al}_{0.3}\text{Ga}_{0.7}\text{As}$ to $\text{Al}_{0.5}\text{Ga}_{0.5}\text{As}$	25nm	UID	0.00E+00	UID
EtchStop	$\text{In}_{0.49}\text{Ga}_{0.51}\text{P}$	50nm	UID	0.00E+00	UID
SCH	$\text{Al}_{0.3}\text{Ga}_{0.7}\text{As}$	50nm	UID	0.00E+00	UID
QW	$\text{Al}_{0.1}\text{Ga}_{0.9}\text{As}$	7 nm	UID	0.00E+00	UID
barrier	$\text{Al}_{0.3}\text{Ga}_{0.7}\text{As}$	5 nm	UID	0.00E+00	UID
QW	$\text{Al}_{0.1}\text{Ga}_{0.9}\text{As}$	7 nm	UID	0.00E+00	UID
barrier	$\text{Al}_{0.3}\text{Ga}_{0.7}\text{As}$	5 nm	UID	0.00E+00	UID
QW	$\text{Al}_{0.1}\text{Ga}_{0.9}\text{As}$	7 nm	UID	0.00E+00	UID
SCH	$\text{Al}_{0.3}\text{Ga}_{0.7}\text{As}$	50nm	UID	0.00E+00	UID
Linearly Graded Region	$\text{Al}_{0.8}\text{Ga}_{0.2}\text{As}$ to $\text{Al}_{0.3}\text{Ga}_{0.7}\text{As}$	100nm	p-type	1.00E+18	p-C
p-doped upper cladding	$\text{Al}_{0.8}\text{Ga}_{0.2}\text{As}$	900nm	p-type	1.00E+18	p-C
Linearly Graded Region	$\text{Al}_{0.1}\text{Ga}_{0.9}\text{As}$ to $\text{Al}_{0.8}\text{Ga}_{0.2}\text{As}$	100nm	p-type	1.00E+18	p-C
p+ doped cap	GaAs	160nm	p-type	2.00E+19	p-Zn
EtchStop	$\text{In}_{0.49}\text{Ga}_{0.51}\text{P}$	200nm	p-type	1.00E+18	p-Zn
Buffer Layer Growth	GaAs	400 nm	n-type	3.00E+18	p-Zn
n-type substrate	GaAs		n-type	>1E18	n-Si
PL wavelength 763nm for lasing wavelength at 780nm					

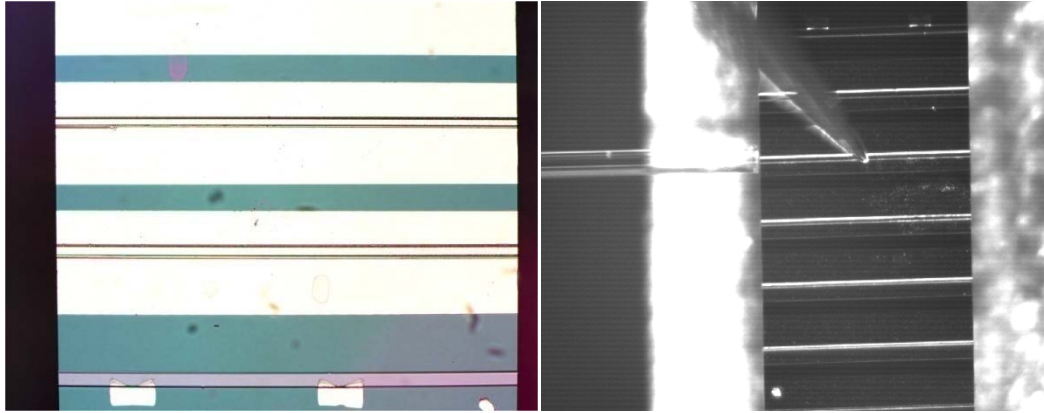


Figure 43 (a) device photo of cleaved broad area laser; (b) measurement setup consists of direct probing and cleaved multimode fiber with 50 μm diameter.

We fabricated a broad area laser by using the proposed wafer stack in Table 3. Figure 43 shows the device and measurement setup under microscope. We used cleaved facet as cavity reflective mirrors and cleaved multimode fiber with 50 μm diameter to collect light from one facet.

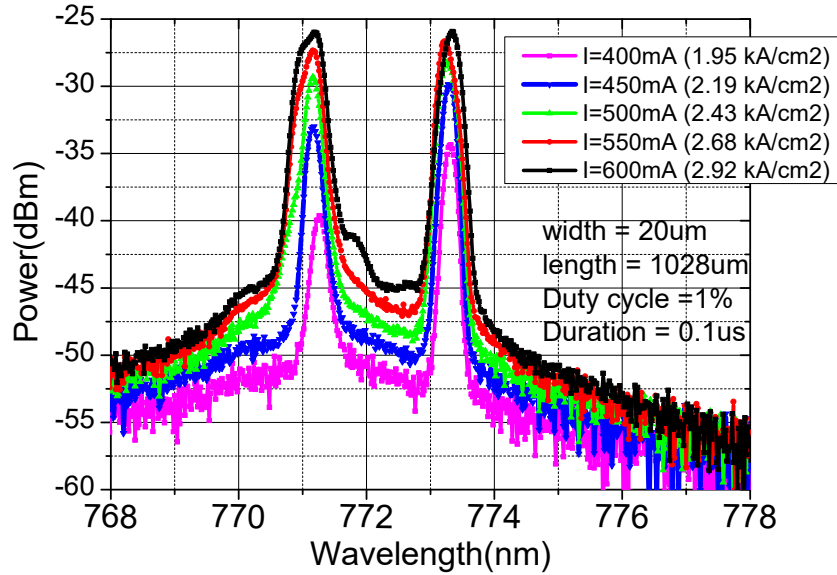


Figure 44 Optical spectrum of broad area laser based by using AlGaAs bonding wafer stack with varying current injection level.

Figure 44 illustrates the spectrum of broad area laser by using AlGaAs bonding wafer stack with varying current injection level from 1.95 to 2.92 kA/cm². The cavity measured is 20 μm wide and 1028 μm long. The driving current used is pulsed current with 1 % duty cycle and 0.1 μs duration. There are more than one lasing peaks shown on spectrum between 770 and 774 nm.

Figure 45 indicates the L-I curve and L-J of a broad area laser with 20 μm width and varying cavity length of 1028, 1138, 1384, and 1520 μm. As shown, threshold current density is about 1.75 kA/cm² for all devices with the same cavity width. In Figure 46, we measured the L-I and L-J curves of 1028, 1138, 1382, 1540 μm length with varying cavity width. As shown in plots, with wider cavity, the threshold current density is smaller, which indicates that the propagation loss is smaller.

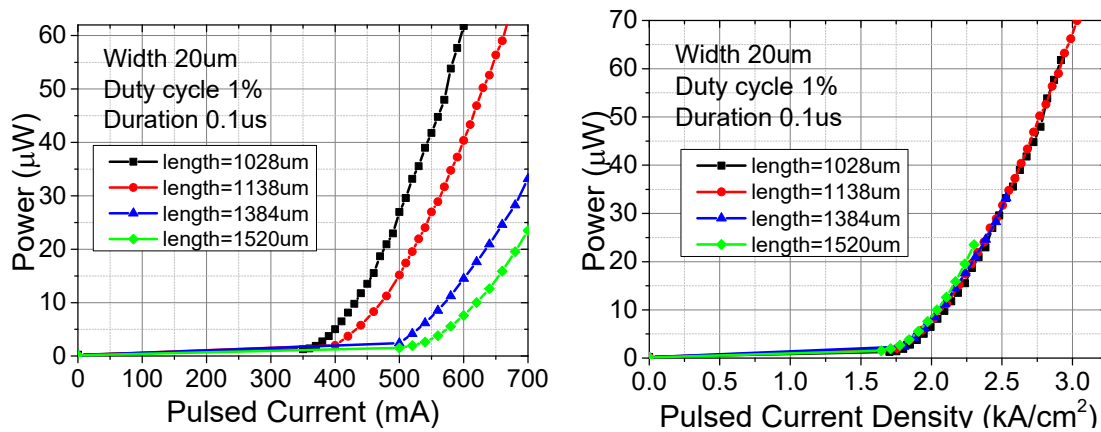


Figure 45 (a) output power collected from broad area laser (both facets) with varying driving current and cavity length; (b) output power collected from broad area laser (both facets) with varying driving current density and cavity length.

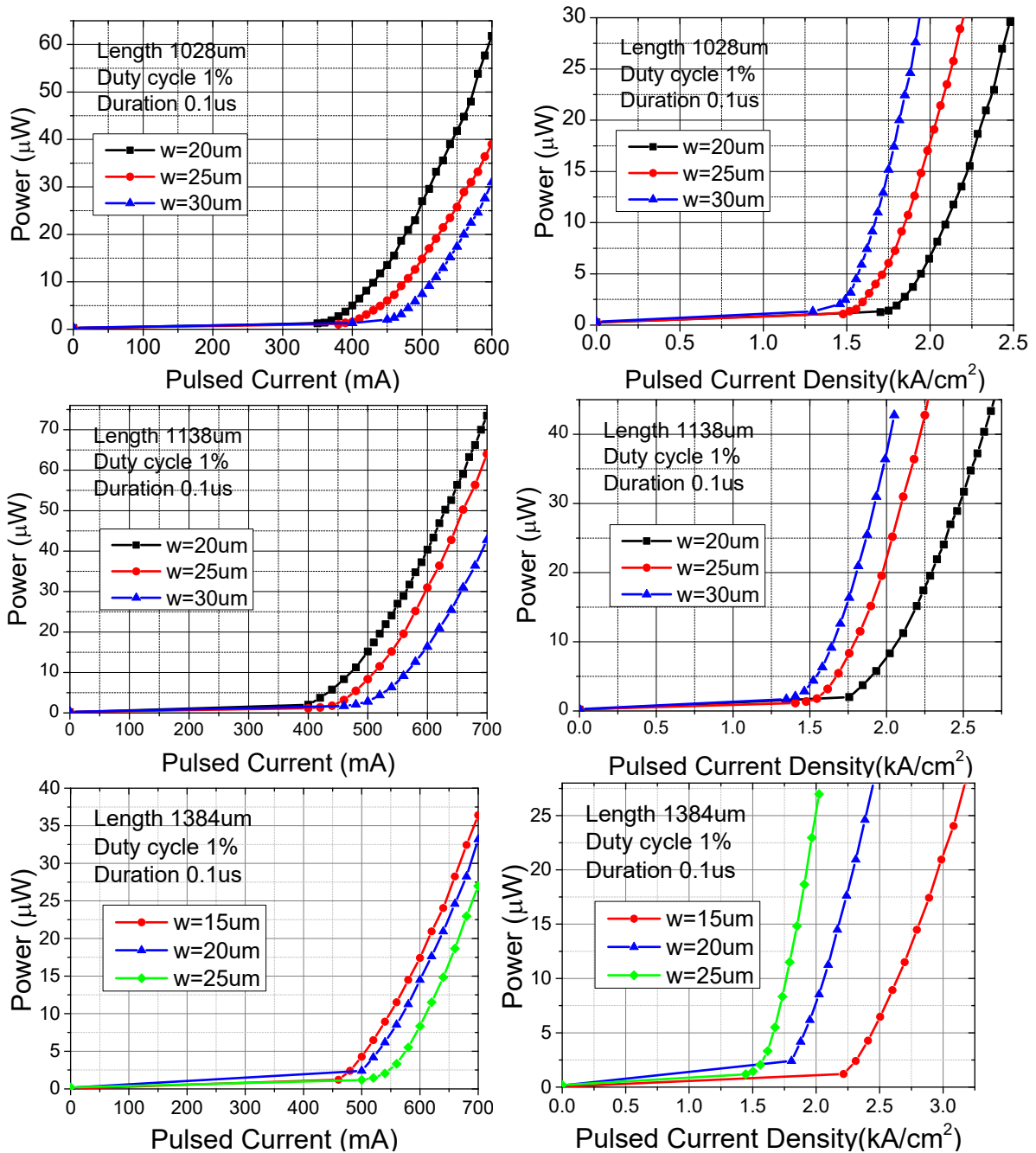


Figure 46 (a-d) output power collected from broad area laser (both facets) with varying driving current and cavity width; (e-h) output power collected from broad area laser (both facets) with varying driving current density and cavity width.

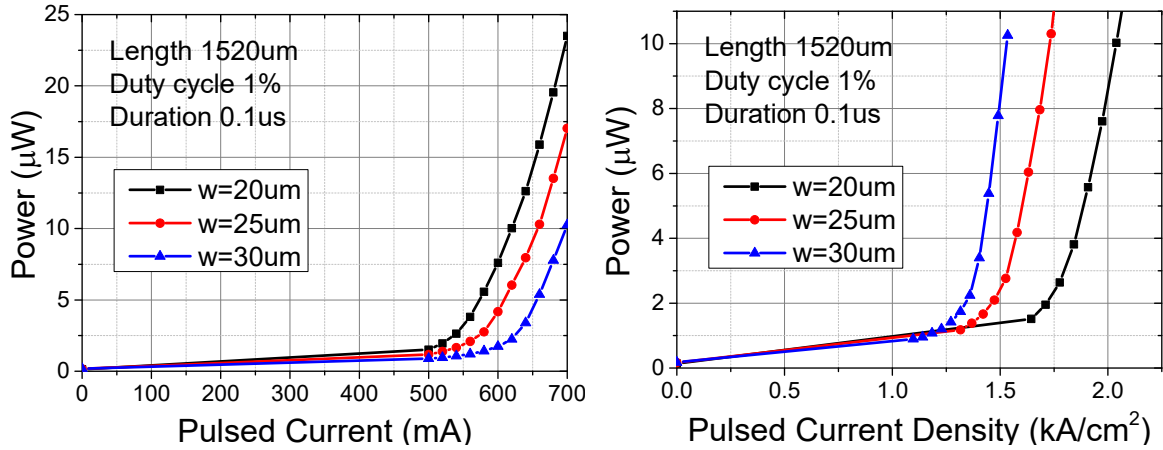


Figure 46 (continued) (a-d) output power collected from broad area laser (both facets) with varying driving current and cavity width; (e-h) output power collected from broad area laser (both facets) with varying driving current density and cavity width.

As shown in the above plots, double lasing wavelengths show up. We investigate the MQWs band diagrams and found slightly band discontinuity in 50 nm InGaP layer. We simulate InGaP etch stop layer with slightly Al doping as shown in Figure 47, Figure 48, and Figure 49 with varying bias voltage.

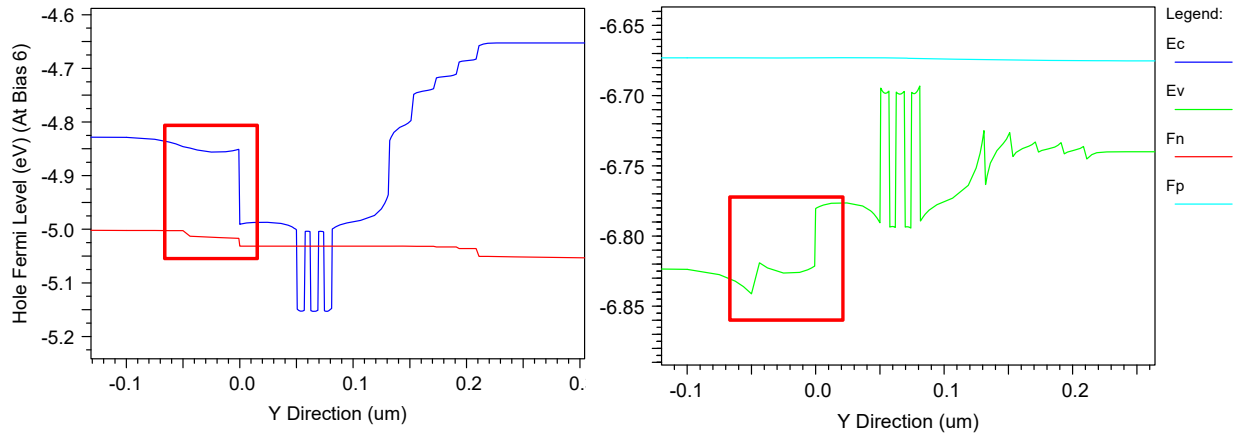


Figure 47 AlGaAs MQWs band diagram with Al_{0.05}In_{0.5}Ga_{0.45}P etch stop layer for (a) Ec; (b) Ev.

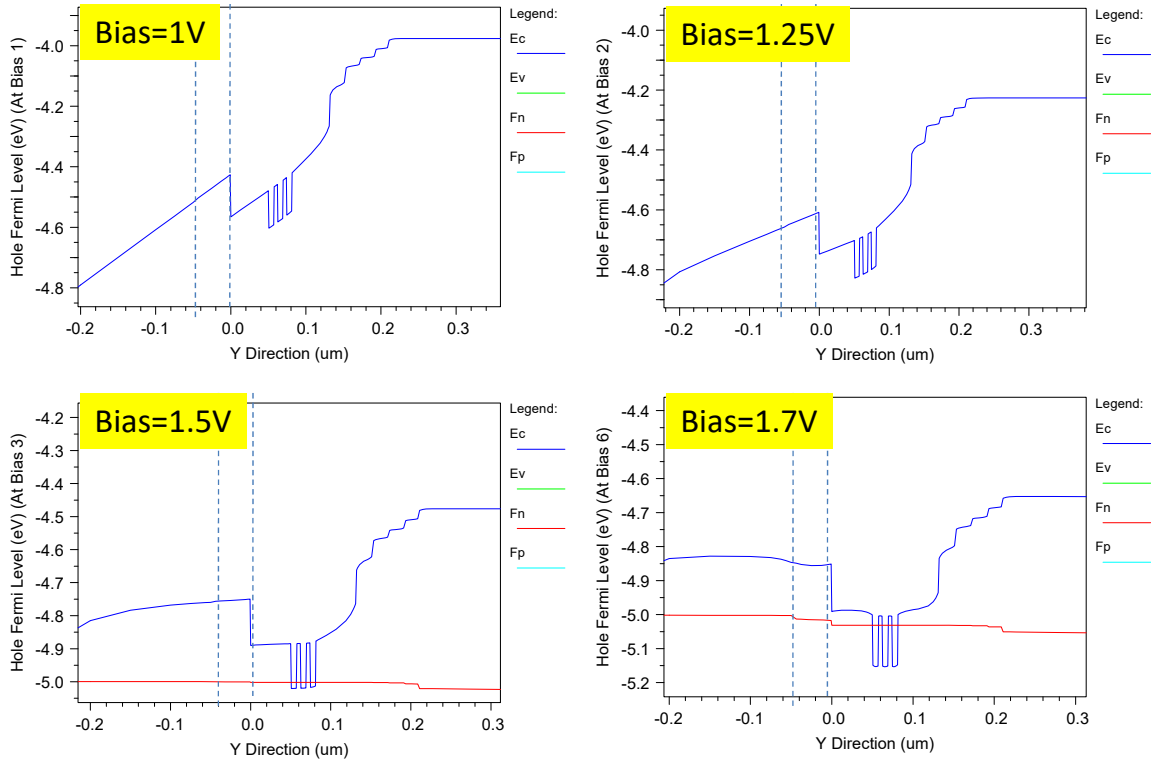


Figure 48. Simulated Ec with $\text{Al}_{0.05}\text{In}_{0.5}\text{Ga}_{0.45}\text{P}$ etch stop layer and varying bias voltage.

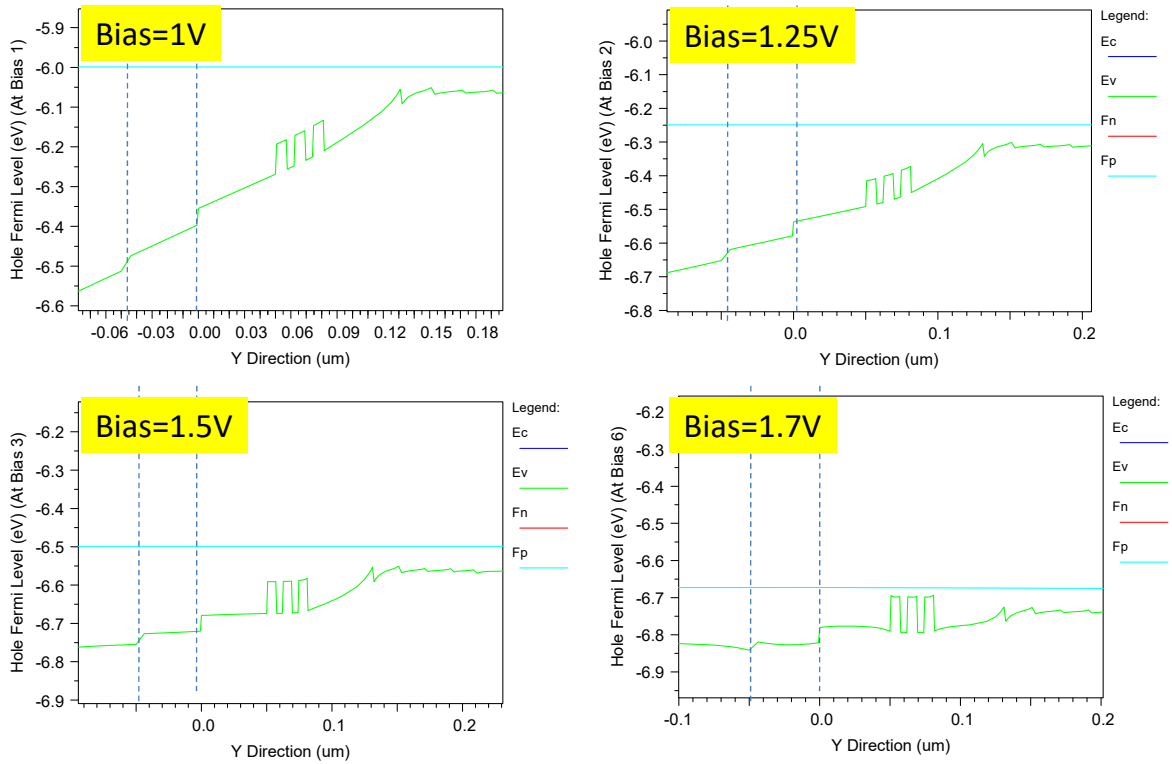


Figure 49. Simulated Ev with $\text{Al}_{0.05}\text{In}_{0.5}\text{Ga}_{0.45}\text{P}$ etch stop layer and varying bias voltage.

Figure 50 shows the proposed fabrication flow charts. We start from AlGaAs III-V epi-wafer, then bond onto 6 inch silicon carrier wafer and release GaAs substrate. The reason to bond III-V wafer onto 6 inch carrier is to utilize our asml300 high resolution lithography tool, which provides 250 nm minimum feature size and less than 60 nm layer-to-layer misalignment.

We define III-V active area and inverse taper by Cl_2/BCl_3 ICP dry etching. By using HCl solution, we can release InGaP etch stop layer above waveguide core. Using the same dry etching, we can define waveguide and N-contact window. PECVD SiO_2 is deposit as isolation layer followed by P-contact and N-contact windows opening. Metal lift-off of Pt/Ti/Pt/Au for 10/40/40/100 nm is used as electrode, finishing with rapid thermal annealing at 380 °C for 30 second.

The active-passive transmission is critical for high-Q ring cavity. We designed double-stage inverse tapers to convert light from active area into passive waveguide. All the simulations are done with assumption of 2 μm P-cladding and N-cladding. The first inverse taper converts mode from P-clad/MQWs/core/N-clad into MQWs/core/N-clad. The p-cladding tapers down to 1 μm , with 100 nm left above MQWs, which is the SCH layer and the linear transition between P-clad and MQWs. Figure 51 illustrates the topview and cross section of the active-passive structure. Figure 52 shows the first and the second order modes confinement, indicating the single mode condition of passive waveguide. The mode converting is shown in Figure 53, with coupling loss of 0.04 dB. The second inverse taper converts mode from MQWs/core/N-clad into core/N-clad. The taper tip width at the end is 250 nm. Figure 54 indicates the mode converting of active-passive transmission. The first inverse taper is not critical regarding tip width, because mode is mainly distributed in MQWs and core. However, for the second inverse taper, the tip width is essential for active-passive transmission due to mode converting from MQWs to core. Thus, we simulated the active-passive transmission with varying inverse taper tip width, as shown in Figure 56. With 250 nm wide inverse taper tip, the active-passive coupling loss is about 0.1 dB. Figure 55 indicates the active waveguide mode profile and single mode condition. Figure 56 simulates the active-passive transmission by 3D FDTD.

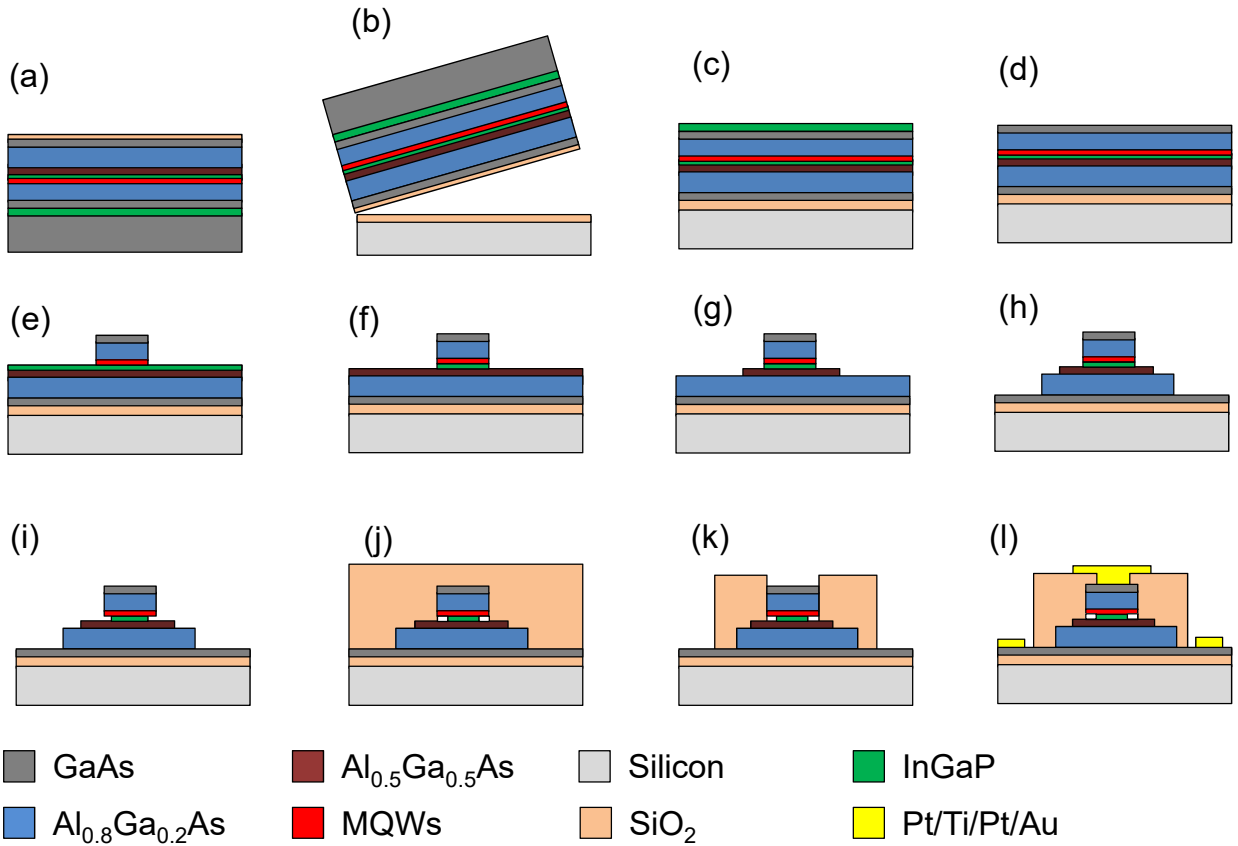


Figure 50 Fabrication flow charts of AlGaAs ring cavity laser active-passive integration. (a) Initial wafer cleaning; (b) direct wafer bonding onto 6 inch silicon carrier wafer; (c) GaAs substrate removal; (d) InGaP etch stop layer removal; (e) III-V dry etching of active area using Cl_2/BCl_3 ; (f) InGaP etch stop layer removal; (g) waveguide dry etching; (h) etching of N-contact window; (i) current window defining (j) PECVD SiO_2 deposition; (k) BOE release P-contact and N-contact windows; (l) P-contact and N-contact metal lift-off.

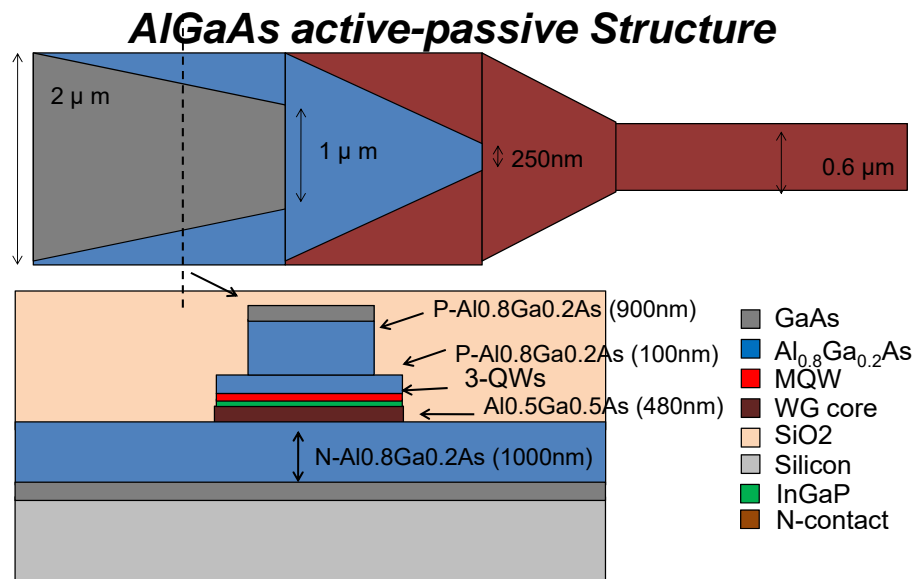


Figure 51 multiple-stage inverse tapers design top view (top) and cross section (bottom).

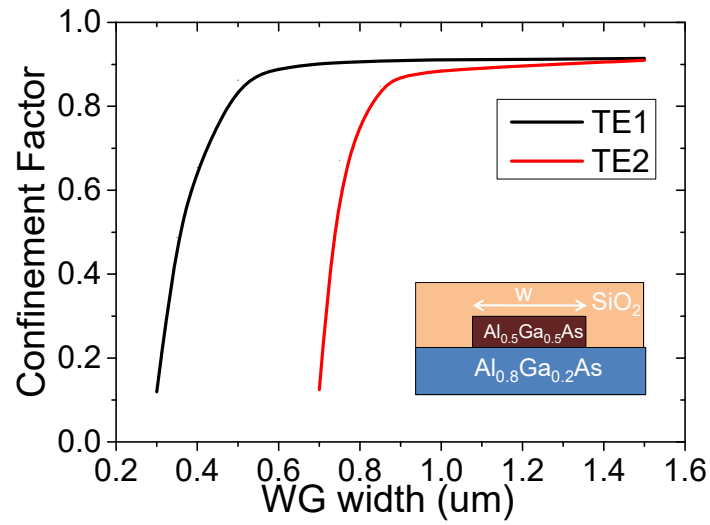


Figure 52 Single mode condition of Al_{0.5}Ga_{0.5}As waveguide with SiO₂/Al_{0.8}Ga_{0.2}As

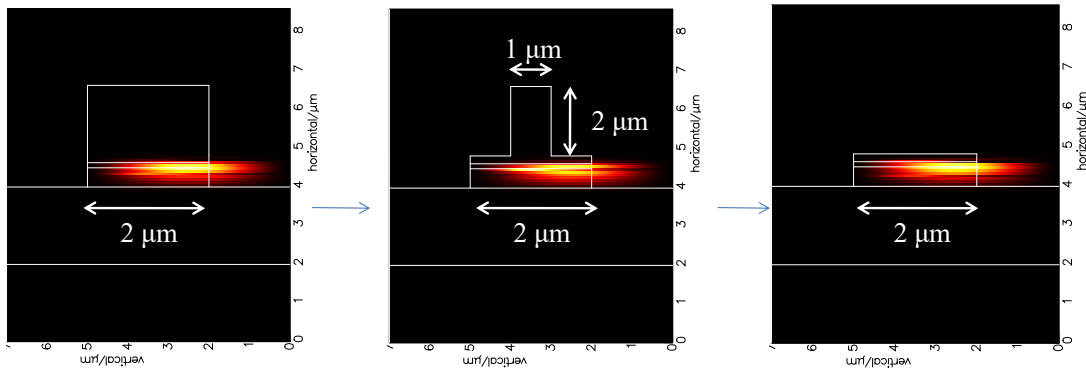


Figure 53 TE mode converting of the first inverse taper.

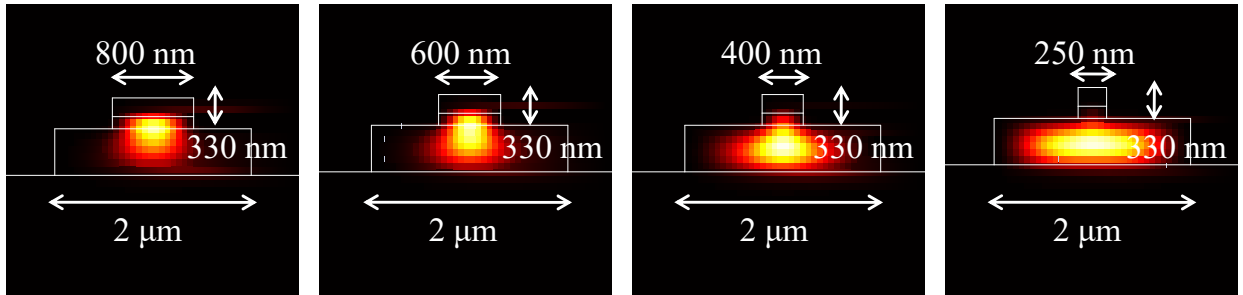


Figure 54 TE mode converting of the second inverse taper.

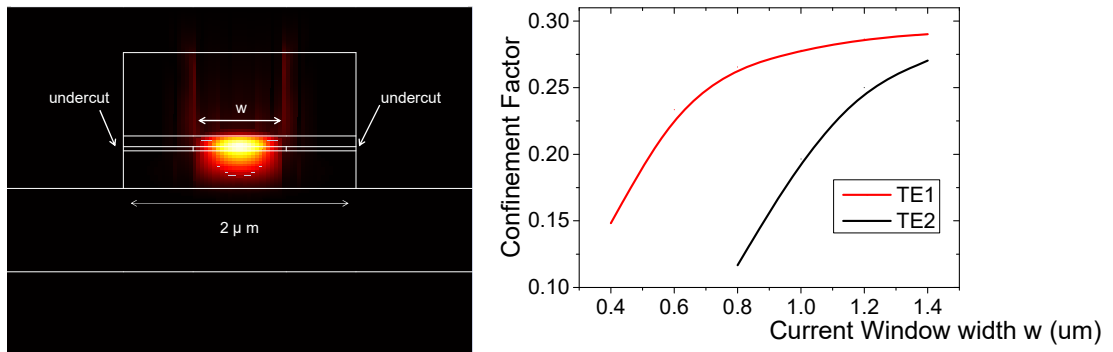


Figure 55 Single mode profile and condition of AlGaAs active layers with InGaP undercut current window.

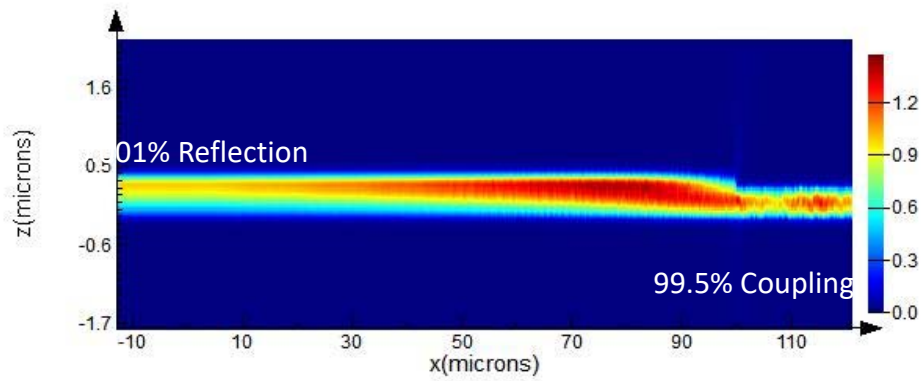


Figure 56 3D FDTD simulation of AlGaAs active-passive transmission.

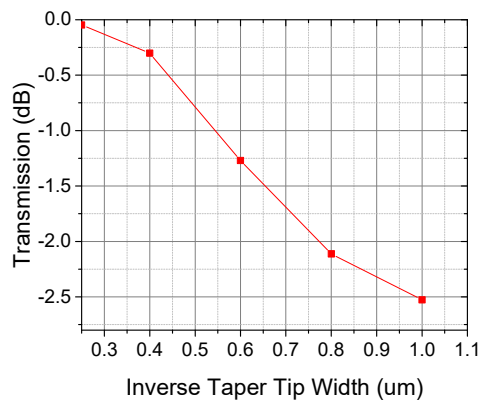


Figure 57 MQWs/core/N-clad to core/N-clad inverse taper transmission with varying inverse taper tip width.

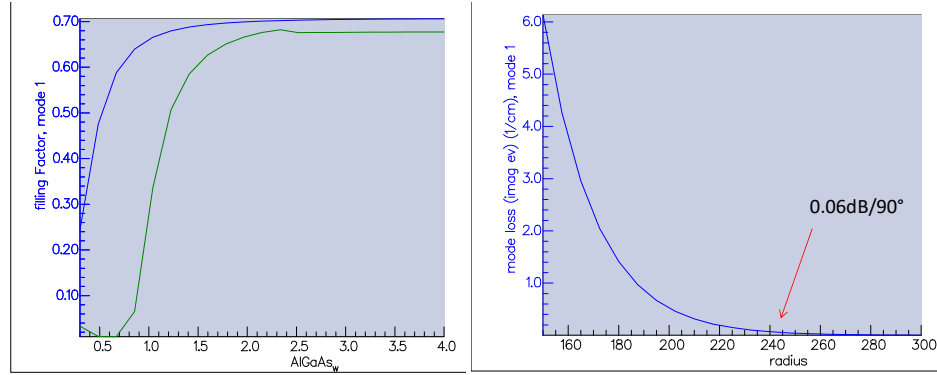


Figure 58 Confinement factor and Bending loss simulation of active waveguides for TE1(blue) and TE2(green).

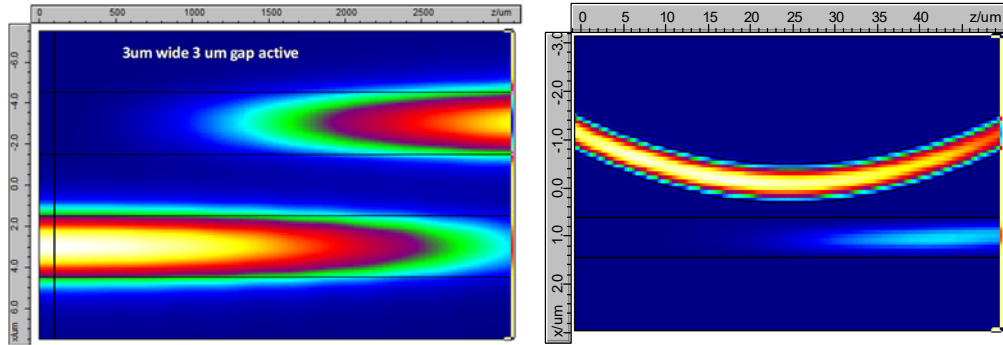


Figure 59 Simulation of passive directional coupler and ring coupler with 0.8 μm width

Table 4 Simulated coupling ratio of ring coupler.

etch depth(μm)	w(μm)	r(μm)	gap(μm)	coupling
1.1	1.2	200	0.3	0.01352466
1.1	1.2	225	0.3	0.01707473
1.1	1.2	250	0.3	0.0203355
1.1	1.2	275	0.3	0.02350146
1.1	1.2	250	0.5	0.00483686
1.1	1.2	250	0.7	0.00105725
1.1	1	250	0.3	0.04694306
1.1	1	250	0.5	0.01243334
1.1	1	250	0.7	0.00305366
1.1	0.8	250	0.3	0.1145457
1.1	0.8	250	0.5	0.03683461
1.1	0.8	250	0.7	0.00933832
1.1	0.6	250	0.3	0.2615777
1.1	0.6	250	0.5	0.1084335
1.1	0.6	250	0.7	0.03469114

Figure 58 illustrates the first order and second order TE mode in proposed waveguide. We use single mode waveguide with width of 1.5 μm and bending radius of 250 μm for 0.06 dB per 90° bending loss. We designed two types of coupler to induce light out from the ring cavity, directional

coupler and ring coupler as simulated in Figure 59. We vary the coupling ratio in the ring cavity design to balance the output power and cavity Q value. With smaller coupling, the Q value of the cavity is larger. Based on the simulation results, we designed the active-passive laser mask of all-active ring lasers, Frequency shifters, and active-passive lasers. Figure 60(a)-(e) indicate the design of all-active laser with ring coupler, all-active laser with directional coupler, double ring all-active laser, unidirectional all-active laser, active-passive laser with directional coupler.

Further, before direct wafer bonding, we have deposited 150 nm SiO₂ on AlGaAs epi wafers by PECVD. We also thermally oxidize 6 inch Silicon wafer for 100 nm at 1000 °C. We use Chemical Mechanical Planarization (cmp) to reduce the surface roughness of PECVD SiO₂ on AlGaAs epi wafer. The RA of the surface after cmp is 0.21 nm. As shown in Figure 62, we took the IR image of the bonded sample and the pair is very well bonded. Also, in addition to direct wafer bonding, we have been working on BCB bonded sample in Figure 63, which indicates the bonding set up and the bonded sample. Afterwards, we lap down the bonded GaAs substrate to 100 μm with no cracks as shown in Figure 67.

Table 5 Simulated coupling ratio of directional coupler

etch depth(um)	w(um)	gap(um)	length(um)	coupling
1.1	1.2	1	1000	0.270749
1.1	1.2	1	800	0.179743
1.1	1.2	1	600	0.104025
1.1	1.2	1	400	0.047202
1.1	1.2	1	200	0.011984
1.1	1.2	1	100	0.003047
1.1	1.2	0.75	500	0.47828
1.1	1.2	0.75	400	0.329145
1.1	1.2	0.75	300	0.195838
1.1	1.2	0.75	200	0.090695
1.1	1.2	0.75	150	0.051863
1.1	1.2	0.75	100	0.023447
1.1	1.2	0.75	80	0.015161
1.1	1.2	0.75	60	0.008689
1.1	1.2	0.75	40	0.00404
1.1	1.2	0.75	20	0.001249
1.1	1.2	0.5	300	0.745401
1.1	1.2	0.5	250	0.582937
1.1	1.2	0.5	200	0.4103
1.1	1.2	0.5	150	0.248634
1.1	1.2	0.5	100	0.116923
1.1	1.2	0.5	80	0.076347
1.1	1.2	0.5	60	0.044029
1.1	1.2	0.5	40	0.020377
1.1	1.2	0.5	20	0.006067
1.1	1.2	0.3	100	0.482257
1.1	1.2	0.3	80	0.332516
1.1	1.2	0.3	60	0.20037
1.1	1.2	0.3	40	0.094541
1.1	1.2	0.3	20	0.02756

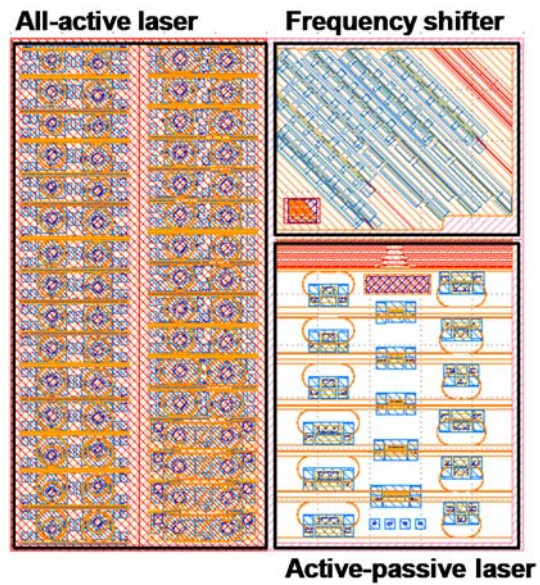


Figure 60 Active-passive Laser layout overview.

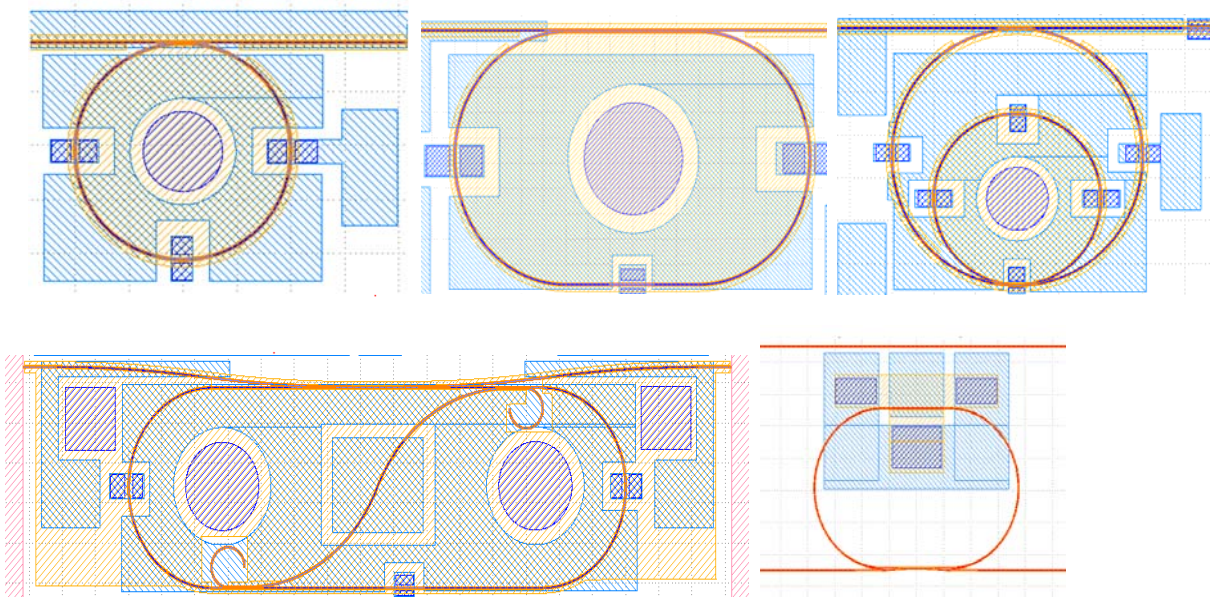


Figure 61 mask layout of active ring, double ring, unidirectional laser, and active-passive ring.

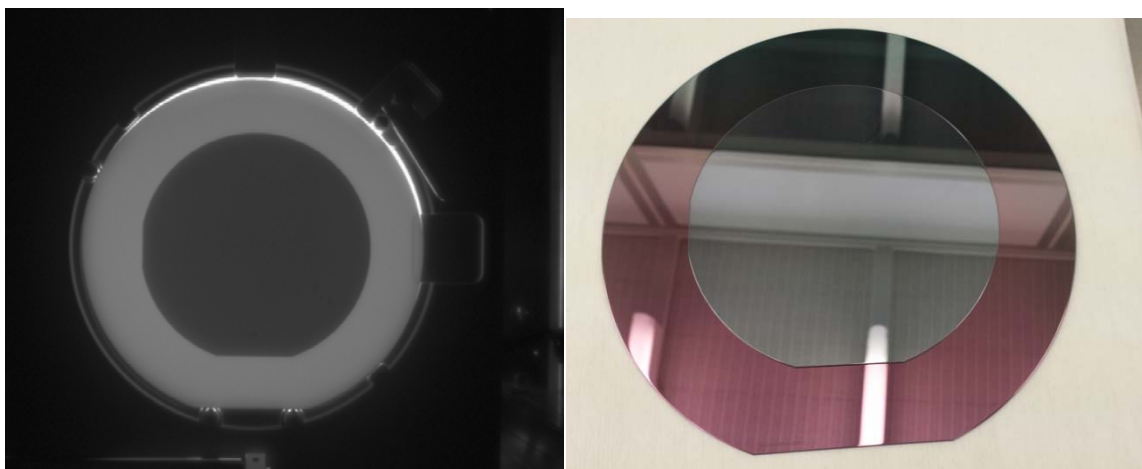


Figure 62 IR image and photo of AlGaAs epi wafer bonded onto 6'' Silicon.

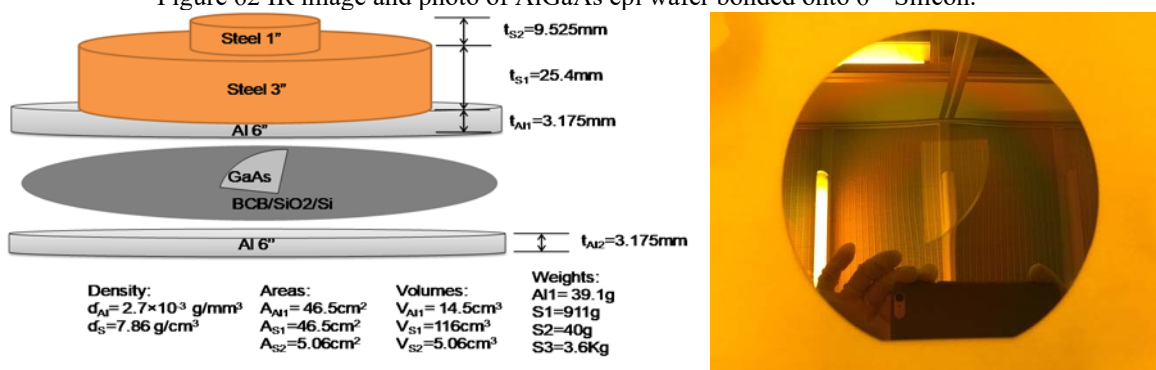


Figure 63 BCB bonding system and bonded sample.

Masimo_M1_6711-2

Cracked and peeled off at 120C

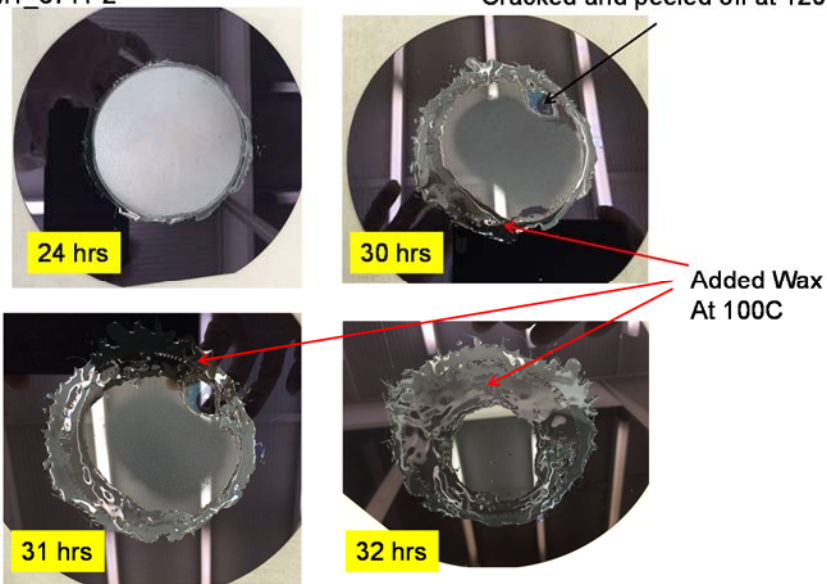


Figure 64 Direct bonded sample GaAs substrate removal by using wet etching.

We use acid of $\text{H}_3\text{PO}_4:\text{H}_2\text{O}_2:\text{H}_2\text{O} = 1:1:8$ to wet etch the GaAs substrate of the bonded wafer. The etching rate on the edge is faster than the center area. We added wax as protection when substrate fully removal from the edges. After 32 hours, in Figure 64, the substrate is fully removed

with more than 90% yielding. As shown in Figure 65, after substrate removal, we used $\text{H}_3\text{PO}_4:\text{HCl}=1:1$ to wet etch 200 nm InGaP etch stop layer. After InGaP removal, the sample surface is clean under Nomarski microscope.

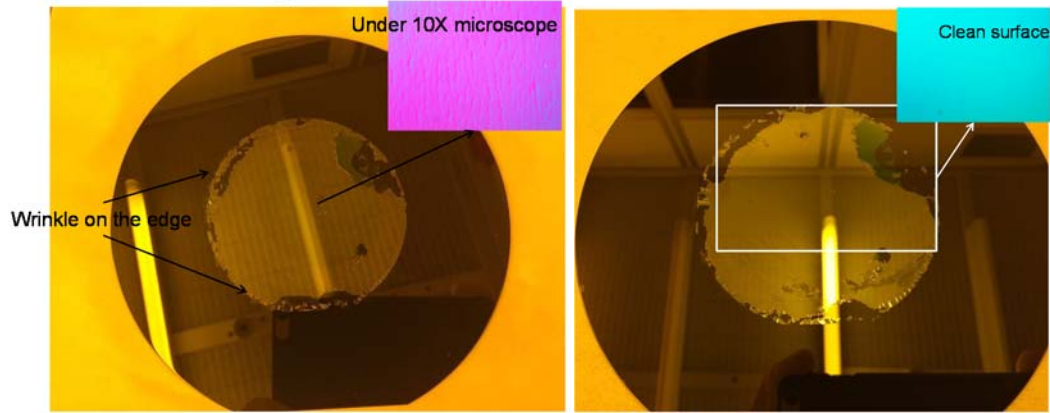


Figure 65 (a) direct bonded epi-sample after substrate removal; (b) direct bonded epi-sample after InGaP etch stop layer removal.

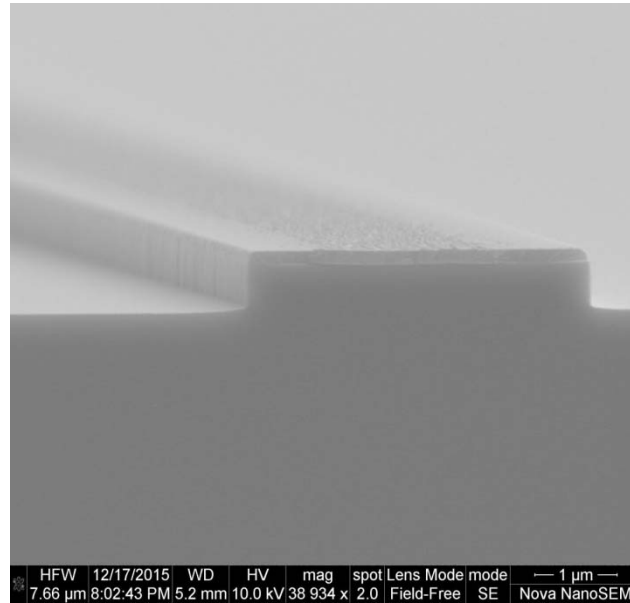


Figure 66 SEM photo of ICP dry etched GaAs waveguide with optimized Cl_2/BCl_2 recipe.

We developed and optimized GaAs dry etching recipe with an ICP dry etching chamber and Cl_2/BCl_3 chemicals. The optimized recipe is listed in Table 6. The etching profiles shown in the SEM photo in Figure 66. We used 200 nm PECVD silicon oxide as hard mask for etching. Figure 67 and Figure 68 are devices photos of fabricated AlGaAs bonding all-active and active-passive lasers.

Table 6. Optimized ICP dry etching of GaAs with Cl_2/BCl_3 .

Pressure(mTorr)	$\text{Cl}_2(\text{sccm})$	$\text{BCl}_3(\text{sccm})$	Sorece Power(W)	Bias Power(W)
10	13	52	1000	40

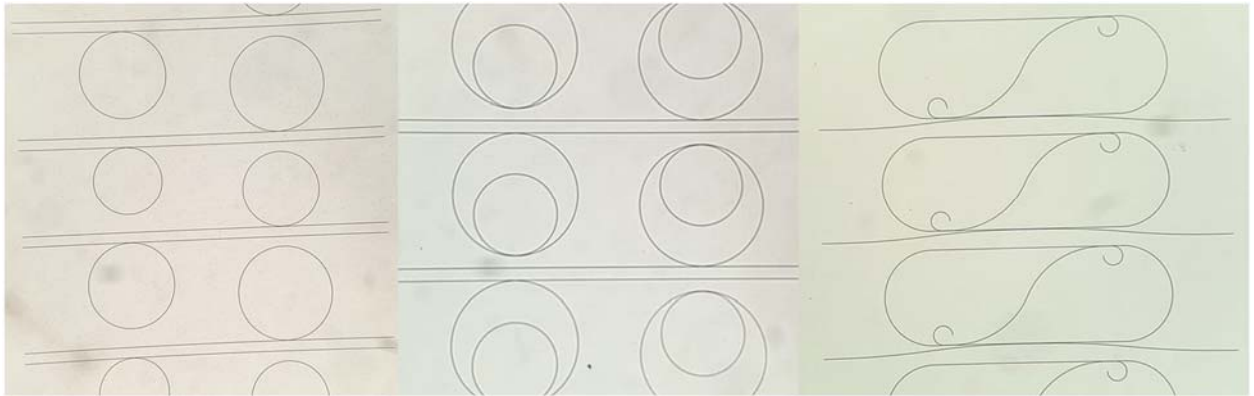


Figure 67 Fabricated AlGaAs laser device photos.

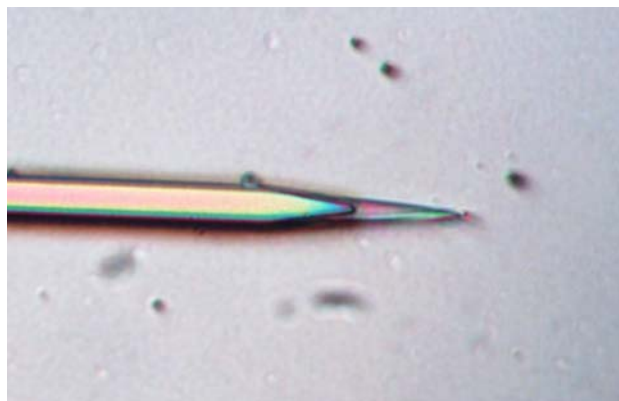


Figure 68 Device photo of fabricated AlGaAs active-passive transmission section.

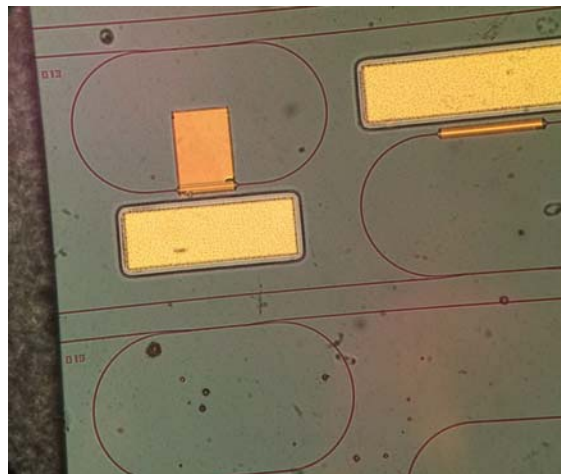


Figure 69 Fabricated AlGaAs laser bonded on silicon with BCB interface.

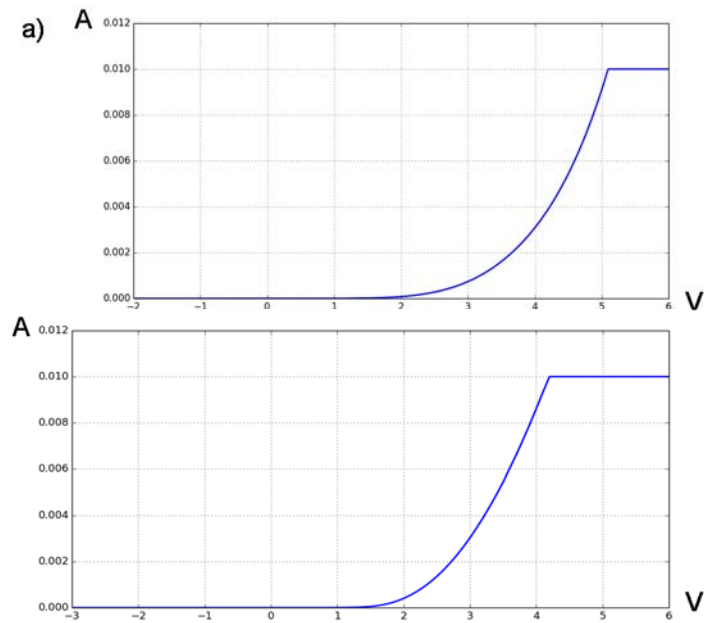


Figure 70 IV curve a) before; b) after RTP process at 250 °C for 30 seconds.

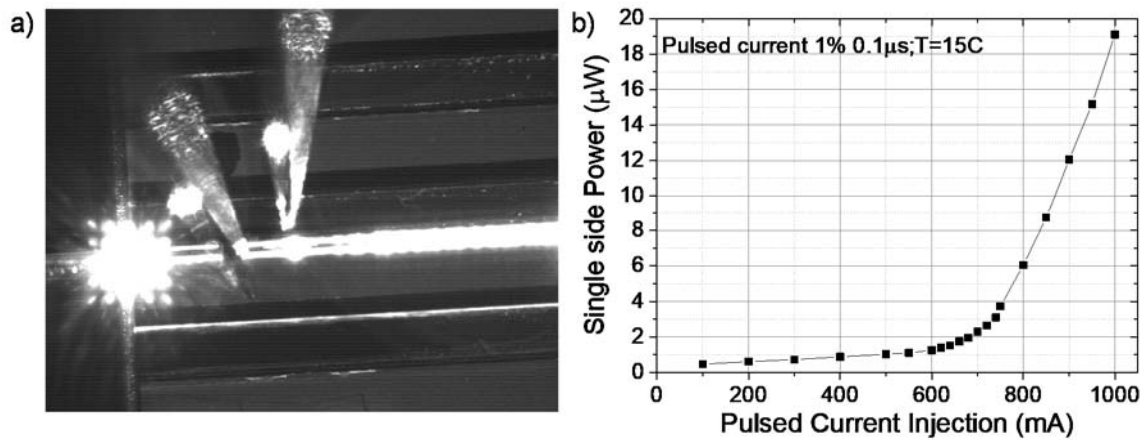


Figure 71 a) The bonded laser device photo with current injection; b) measured L-I curve of the straight cavity AlGaAs bonding laser with BCB interface.

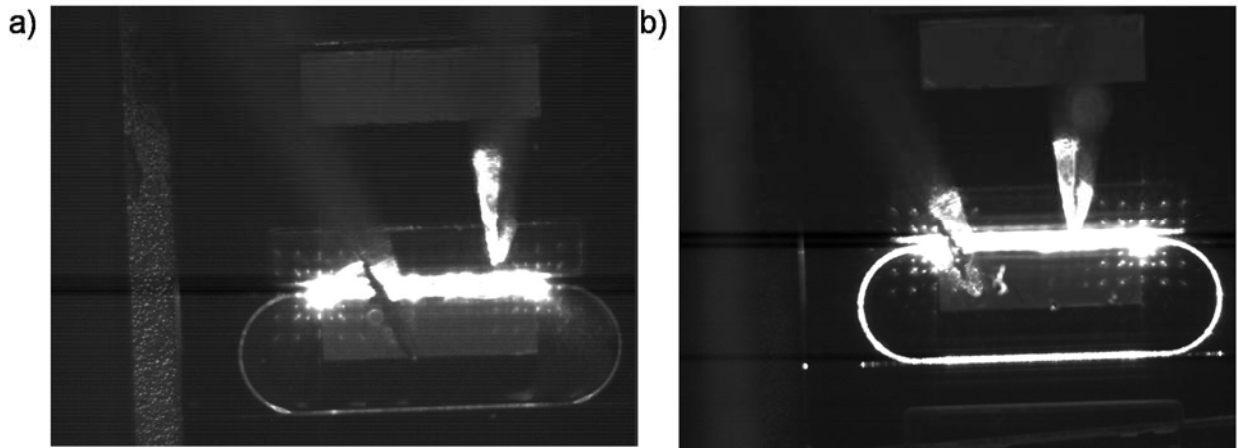


Figure 72 Device photos of AlGaAs bonding laser with BCB interface and a) SiO2 cladding; b) TiO2 cladding.

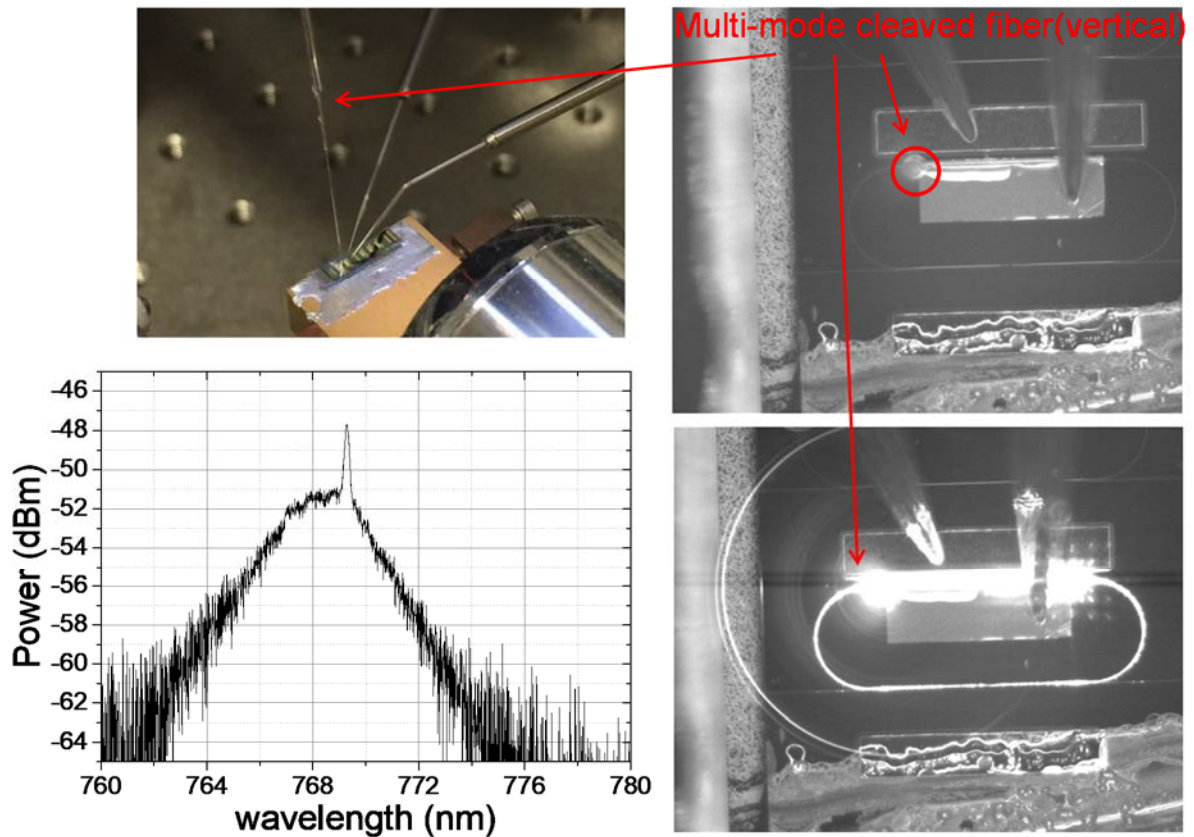


Figure 73 The device photos of ring cavity AlGaAs bonding laser with BCB interface and spectrum collected by vertically mounted multimode cleaved fiber.

We finished the fabrication of AlGaAs laser bonded on silicon with BCB interface. Figure 69 shows the fabricated devices. We investigated the rapid thermal process (RTP) with the BCB bonded AlGaAs devices and found that the bonding interface can survive under 250 °C for 30 seconds. We proceed with the process for electrodes annealing. Figure 70 indicates the diode IV curve before and after RTP. Afterward, we measured the straight cavity bonding laser. Figure 71 shows the device photo of AlGaAs bonding laser with current injection and the measured IV curve.

We verified the result with Figure 45, where the laser was not demonstrated on a bonding structure. We conclude that with the similar current injection level, the straight cavity laser share the same emission efficiency with or without bonding.

We proceed with the testing of ring cavity active-passive AlGaAs bonding laser with BCB interface. Figure 72 shows that active-passive transmission is low with SiO₂ cladding due to the refractive index contrast. To increase the cladding index, we removed SiO₂ cladding and deposit TiO₂ cladding by RF magnetron sputtering, which has refractive index of 2.0. With TiO₂ cladding, the active-passive transmission increases. Figure 73 shows the spectrum and the measurement setup we used for testing, where a multimode cleaved fiber was mounted vertically and collected light from the top.

III.1. Publications

- "Single-tone optical frequency shifting and non-magnetic optical isolation by electro-optical emulation of a rotating half-wave plate in a traveling-wave lithium niobate waveguide", Chuan Qin, Hongbo Lu, Burcu Ercan, Siwei Li and S. J. Ben Yoo, *IEEE Photonics Journal*, vol. 9 issue 3 2017
- "Power-efficient electro-optical single-tone optical-frequency shifter using X-cut Y-propagating lithium tantalate waveguide emulating a rotating half-wave-plate", Chuan Qin, Hongbo Lu, Andrea Pollick, Sri Sriram and S. J. Ben Yoo, *Optical Fiber Communication Conference (OFC)*, 2017
- "ZnO-diffused lithium niobate waveguide polarization controller," Paper 9750-6, James E. Toney, Andrea Pollick, Jason Retz, Vincent E. Stenger, Sri Sriram, SRICO Inc, SPIE Photonics West, 2016.
- Ph.D. Thesis: Kuanping Shang, "Heterogeneous Integration and Multilayer Platform for Photonic Integrated Circuits," University of California, Davis, September 30, 2017
- Ph.D. Thesis: Chuan Qin, "Technologies for Elastic Optical Networking Systems in Spatial, Temporal and Spectral Domains," University of California, Davis, September 30, 2017

IV.2. Inventions and Patents

Patent Application

Sung-Joo Ben Yoo, Chuan Qin, Burcu Ercan, Hongbo Lu, UC17-363-1PSP, CRYSTAL-ORIENTATION-OPTIMIZED OPTICAL FREQUENCY SHIFTER WITH OPTICAL POLARIZATION CONVERSION AND OPTICAL ISOLATION CAPABILITY

III.3. Students and Postdocs Supported

Chuan Qin (Ph D student, PhD received September 2017)

Tiehui Su (Ph D student, PhD received September 2017)

Burcu Ercan (Ph D student)

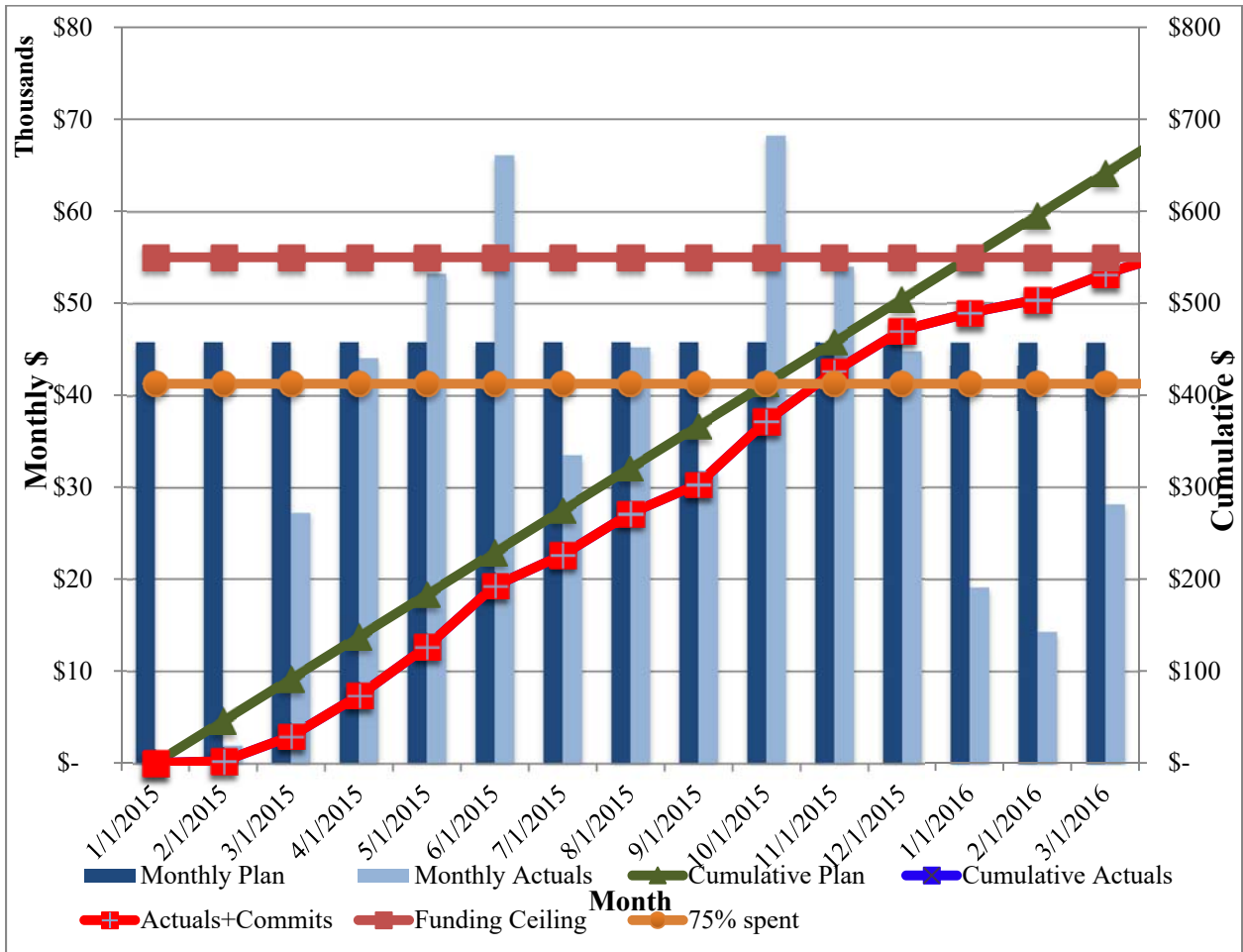
Mathias Prost (Postdoc researcher)

(No undergraduate students)

III.4. Summary

This project report summarizes the UC Davis-led CAMS project that covers progress on coherent frequency shifter, optical isolator, and lasers at 780 nm wavelength. The LiNbO₃ based coherent optical frequency shifter worked as a single tone high extinction frequency up shifter/down shifter while it also achieved high extinction optical isolators. The ring laser achieved room temperature cw operations at 780 nm. The summary of the key achievements are as follows: (1) Successful experimental demonstration of single tone frequency shifting with extinction 20 dB, (2) experimental demonstration of frequency shifting with continuous sweeping from +/- 2.5 GHz frequency shifts with potential capability to achieve beyond +/- 10 GHz; (3) experimental demonstration achieving frequency shifting with 20 dB optical isolation; (4) experimental demonstration achieving frequency shifting with < 10 % leakage; (5) experimental demonstration achieving frequency shifting with < 3 dB forward optical loss; (6) 29.3 dBm RF power operation of optical frequency shifter; (7) a new design and theoretical analysis of frequency shifter with larger electro-optical coefficients demonstrating 2.85× reduction of required voltage (7.2× power reduction); (8) Room temperature cw operation of broad area 780 nm laser fabricated using AlGaAs MQWs bonding wafer stack with InGaP etch stop layer calibrating lasing wavelength and LI-curves; (9) Development of AlGaAs active-passive laser fabrication processes including optimized wafer bonding and AlGaAs dry etching recipe; (10) Fabrication of the new 780 nm AlGaAs active-passive integrated laser.

III.5. Financial Report



References

- [1] R. Noe and D. A. Smith, "Integrated-optic rotating waveplate frequency shifter," *Electronics Letters*, vol. 24, pp. 1348-1349, 1988.
- [2] S. Ninshimura, H. Inoue, and S. Tanaka, "A Semiconductor Waveguide-Type Optical Frequency Shifter," *Optical Review*, vol. 2, pp. 229-232, 1995/08/01 1995.
- [3] C. Qin, H. Lu, A. Pollick, B. Ercan, J. E. Toney, J. Retz, V. E. Stenger, S. Sriram, and S. J. B. Yoo, "Single-tone optical frequency shifting and non-magnetic optical isolation by electro-optical emulation of a rotating half-wave plate in a traveling-wave lithium niobate waveguide," *Optics Express*, (submitted), 2016.

DISTRIBUTION LIST

DTIC/OCF	
8725 John J. Kingman Rd, Suite 0944	
Ft Belvoir, VA 22060-6218	1 cy
AFRL/RVIL	
Kirtland AFB, NM 87117-5776	1 cy
Official Record Copy	
AFRL/RVBYE/Dr. Brian Kasch	1 cy